aerospace

MDPI

Article

Sizing Methodology and Energy Management of an Air–Ground Aircraft with Turbo-Electric Hybrid Propulsion System

Mingliang Bai [1], Wenjiang Yang [1,*], Jianwei Li [2], Marek Kosuda [3], Ladislav Fozo [3] and Miroslav Kelemen [3]

[1] School of Astronautics, Beihang University, Beijing 100191, China
[2] National Engineering Laboratory for Electric Vehicles, Beijing Institute of Technology, Beijing 100081, China
[3] Faculty of Aeronautics, Technical University of Kosice, 04121 Kosice, Slovakia
* Correspondence: yangwjbuaa@buaa.edu.cn; Tel.: +86-13691115160

Abstract: This paper proposes a distributed turbo-electric hybrid propulsion system (TEHPS) architecture for high-power and large-load air–ground aircraft (AGA). The composition of the turboshaft engine, hybrid energy storage system (HESS) as the power unit, distributed electric drive ducted fans, and wheels as the propulsion unit is determined. Firstly, the modeling of each component in the TEHPS is carried out, and system power, energy, and weight analysis are conducted under the different operating modes. Sizing parameters of main components are selected based on a genetic algorithm to obtain the optimal total weight and propulsion efficiency, and the energy management framework from the upper level to the lower level is completed by adopting an equivalent consumption minimum strategy and fuzzy logic control. Under the air–ground amphibious mission profile, the simulation results indicate that the TEHPS can achieve a 21.80% fuel consumption and CO_2 emission optimization rate at the cost of 10.53% increase in the whole aircraft mass compared to the oil-only powertrain. The HESS can account for up to 29% and 33.56% of the energy and power ratios in the TEHPS, and reduce mass by 8.1% and volume by 3.77% compared to the single energy storage, which may provide theoretical insights for the powertrain composition form, sizing, and energy management of future hybrid air–ground aircraft.

Keywords: air–ground aircraft; distributed electric propulsion; energy management; hybrid energy storage system; size optimization

Citation: Bai, M.; Yang, W.; Li, J.; Kosuda, M.; Fozo, L.; Kelemen, M. Sizing Methodology and Energy Management of an Air–Ground Aircraft with Turbo-Electric Hybrid Propulsion System. *Aerospace* **2022**, *9*, 764. https://doi.org/10.3390/aerospace9120764

Academic Editor: Konstantinos Kontis

Received: 19 October 2022
Accepted: 25 November 2022
Published: 28 November 2022

1. Introduction

With the significant growth in travel and transport demand in the aviation and traffic industries, electrified transportation and energy conservation have become an inevitable trend. Major carbon emitting countries such as the United States, the European Union, and China have put forward plans and solutions for energy saving and carbon reduction in an effort to achieve carbon peak and carbon neutrality [1–3]. Facing the problems of high ground traffic pressure, complex road conditions, and hostile field environments, integrated air–ground mobility that can be operated both in the air with propulsion units and on the ground via wheels is a promising solution [4]. In recent years, vertical take-off and landing air–ground aircraft (AGA) with various propulsion forms have been a hot topic for car and aircraft manufacturers and civil and military research institutes [5–7], including the Vahana [8], City Airbus [9], and Joby Aviation Air Taxi [10] with electric propulsion; Transition and TF-2 [11] with hydrocarbon fuel; and Nexus [12] and WD-1 [13] with hybrid power. However, AGA with all-electric propulsion usually have a maximum take-off weight of no more than 1 tonne and carry only 1–2 passengers.

Large-payload, high-performance amphibious AGA should require an advanced power system to meet the high-power extraction requirements, making a hybrid propulsion system (HPS) the prime choice [14,15]. The employment of conventional internal

combustion engines (ICE) results in increased energy consumption and environmental pollution due to fuel calorific value limitations [16]. Owing to the high power, superior power density, and better structural compactness compared to the ICE, the turboshaft engine can replace it as the main power source for HPS [17,18]. Donateo et al. carried out a control-based dynamic modeling approach using a two-spool turboshaft engine for hybrid urban air mobility (UAM), validating its superiority in the parallel hybrid system architecture [19]. The turbine generation system (TGS), integrated turboshaft engine, and generator have become significant technical support for the application and development of high-power HPS [20].

As an energy buffer in HPS, an energy storage system (ESS) can output or absorb power during the specific flight phase. However, its energy and power densities fail to reach the levels of fossil fuels, inevitably leading to an increase in the share of weight associated with propulsion energy. Hybrid energy storage systems (HESS) can combine the advantages of a high energy-based medium and a high power-based medium for the purpose of reducing system weight [21,22]. Nicola et al. carried out a performance comparison analysis of energy storage systems for light twin-propeller aircraft and demonstrated that the HESS can reduce weight by approximately 43% compared to the ESS and can better cope with peak power demands during the vertical take-off and landing (VTOL) [23]. Therefore, this paper combined the benefits of the TGS and HESS on the basis of the HPS and proposed the turbo-electric hybrid propulsion system (TEHPS) for hybrid air–ground aircraft (HAGA). The series architecture was selected, comprising the turboshaft engine, generator, hybrid energy storage system with lithium batteries and supercapacitors, and distributed electric drive-propulsion units.

Complicated power systems can be costly, energy-intensive, and polluting, requiring reasonable size optimization and effective energy management for AGA. However, the current studies have focused on path planning [24,25] and data communication [26]. The take-off weight of the HAGA is impacted by the number of batteries and supercapacitors, which directly determines the auxiliary energy and power of the TEHPS. Due to the presence of distributed electric propulsion-drive units, the energy conversion efficiency is also an important indicator for the evaluation of such propulsion architecture. Therefore, balancing the take-off weight of the HAGA with the energy and power requirements, while considering the optimum energy conversion efficiency, is the challenge of sizing optimization for the TEHPS.

Sizing methodology for hybrid-electric aircraft (HEA) can provide the foundation and theoretical experience. The genetic algorithm (GA) can overcome the disadvantages of gradient-based optimization algorithms, which have to calculate the derivatives of the objective function and tend to fall into local optimum, and are widely applied to the optimal design of complicated systems that consider a large number of parameters [27]. Xie et al. proposed a benchmark non-dominated sequencing algorithm for the retrofit of a mid-scale HEA to achieve an optimal trade-off between fuel consumption and flight time, and the 17.6% fuel optimization rate was achieved without compromising range [28]. Economou et al. also carried out the power source component selection of a light aircraft using a non-dominated sequencing algorithm, with other components using GA to minimize weight [29]. The possibility of combining distributed electric propulsion with more-electric aircraft concepts to improve aircraft performance has been demonstrated in this literature [30]. As for general aviation aircraft, the initial design approach was oriented towards the optimization objectives of minimum mass, primary energy consumption, and cost, and was used to determine the power-to-weight ratio, wing loading and hybridization of series and parallel systems [31,32]. Facing the demands of dual-purpose for urban air mobility and military transport, Chakraborty et al. developed an adaptable parametric energy-based aircraft configuration evaluator to research the parametric definition and dimensional evaluation of the hybrid tilt-wing and ducted fan lift-plus-cruise aircraft [33,34]. Moreover, Lee et al. proposed a generic conceptual design methodology applicable to various hybrid-electric VTOL aircraft, including the comprehensive flight-analysis module,

HPS sizing module, mission-analysis module, and weight-estimation module [35]. Wang et al. proposed an adaptive and enhanced hypotrochoid spiral optimization algorithm for HAGA to find the optimal sizing of the energy storage system and the logical threshold control parameters of the turboshaft engine [36]. This co-optimization strategy reduced the initial weight by 5.08%, fuel consumption by 26.10%, and battery degradation by 2.08%, providing theoretical insights into HAGA powertrain sizing [37].

The multi-dimensional energy management framework is particularly critical due to the complex configuration of the power system, combined with the nonlinear time-varying nature of the HAGA. Energy management strategies (EMSs) for hybrid propulsion systems involve rule-based control and optimization-based control methods, the former is represented by a state machine (SM), fuzzy logic control (FLC), and power following control (PFC), while the latter is embodied by dynamic programming (DP), Pontryagin's minimum principle (PMP), model predictive control (MPC), convex programming (CP) and equivalent consumption minimum strategy (ECMS). EMSs based on rule-based control with SM [38,39], FLC [40] and PFC [38] are validated in a hybrid unmanned aerial vehicle (UAV) with the fuel cell as the main power source to rationally distribute demand power and reduce hydrogen consumption. Donateo et al. proposed and improved an online energy management strategy based on DP and FLC for the UAM hybrid-electric air-taxi, reducing fuel consumption by 11% taking into account battery degradation [41]. In addition, by applying DP to four different missions of a hybrid-electric helicopter, quantifying the fuel-saving potential, and setting control benchmarks, fuel optimization rates of 10–24% can be achieved [42,43]. PMP can convert the global-optimum problem into a local-optimum problem and is validated for the energy and thermal management of hybrid turboelectric aircraft, reducing the computational effort compared to the benchmark DP [44]. MPC [45] and CP [46] formulate energy management as a convex optimization problem, taking into account vehicle mass variations and predicting future component parameters for a finite period, which can reduce computation time compared to DP and is more suitable for real-time supervisory control [47]. Furthermore, ECMS introduces the Hamiltonian function and equivalent factor to transform the global problem into an instantaneous optimization problem. It can be integrated with upper-level particle swarm optimization (PSO) to form a bi-level HPS multi-objective optimization scheme [48], and with FLC to formulate a composite energy management strategy to maintain the battery state of charge (SOC), achieving less fuel consumption, less computation time and control values fluctuation [49,50]. On the whole, the TEHPS energy management is mainly aimed at the main power unit TGS and the auxiliary power unit HESS. However, in order to demonstrate the high power density and energy density characteristics of the HESS, the lower-level power distribution should be carried out within the HESS for the battery pack and supercapacitor pack.

In order to overcome the lack of power and performance of existing AGA, a solution is proposed for a high-power TEHPS containing a turboshaft engine and a hybrid energy storage system. Energy analysis, power calculation, and mass evaluation of the HAGA are first carried out, and research on size optimization and energy management of the TEHPS is performed. Multi-objective optimization is conducted based on the genetic algorithm for initial system weight and electric propulsion efficiency. A hierarchical energy management framework is developed for an air–ground amphibious mission profile and ECMS and FLC are applied to the TEHPS and HESS respectively, to optimize fuel economy, power, and emissions performance. The rest of this paper is organized as follows: the models of turbo-electric hybrid propulsion systems are established in Section 2. The descriptions of power, energy, and weight analysis for HAGA are introduced in Section 3. In Section 4, the size optimization method and energy management framework are developed. In Section 5, simulation verification and result analysis under a specific flight condition are carried out. Finally, the conclusion is drawn in Section 6.

2. Model of Turbo-Electric Hybrid Propulsion System

Turbo-electric hybrid propulsion systems can be divided into power storage ports and load ports according to the generation and utilization of electrical energy. Specifically, the power storage port consists of the turbine generation system and hybrid energy storage system, and the load port embodies the distributed electric drive-propulsion units. The various views of HAGA in different directions are shown in Figure 1, and the TEHPS powertrain architecture and basic parameters are visible in Figure 2 and Table 1.

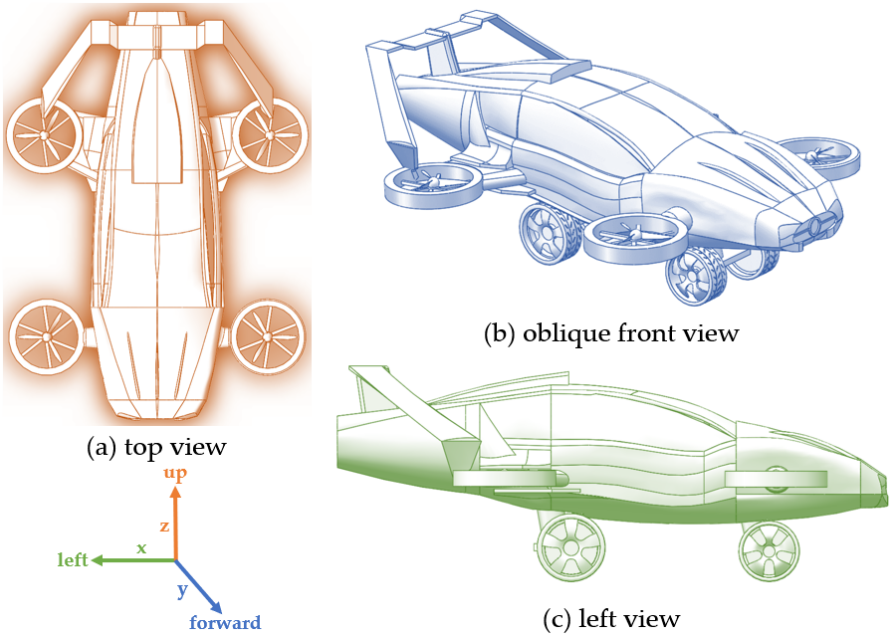

Figure 1. Three views of hybrid air–ground aircraft in different directions.

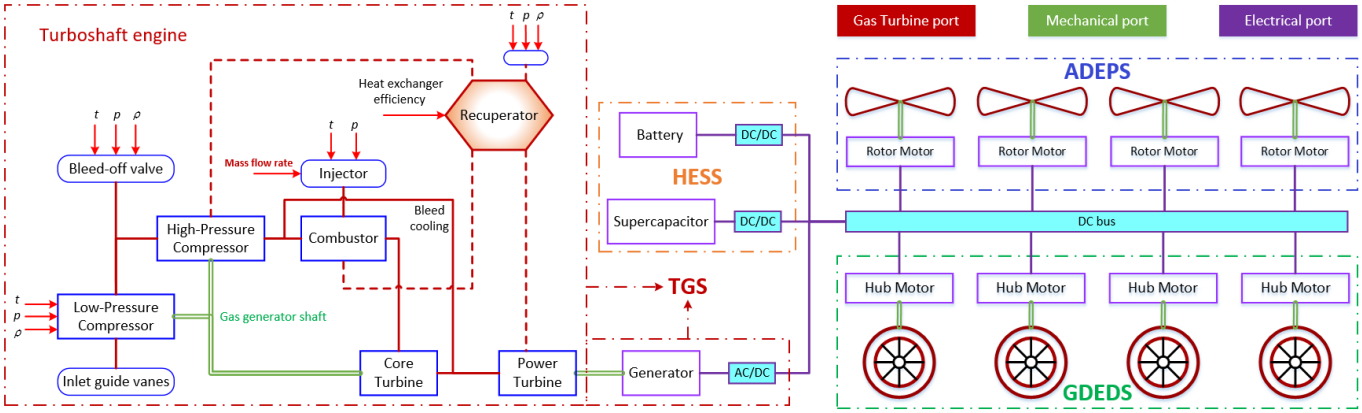

Figure 2. Powertrain architecture of turbo-electric hybrid propulsion system in HAGA.

Table 1. Basic parameters of hybrid air–ground aircraft.

Title	Value	Mode	Title	Value	Mode
Gravity acceleration g	9.8 m/s^2	Air/ground	Wheel radius	0.4/0.25 m	Ground
Rolling resistance coefficient C_r	0.02	Ground	Transmission efficiency	1	Ground
Air drag coefficient C_{ad}	0.5	Air/ground	Aircraft mass	2000 kg	Air
Active area S	8.75 m^2	Ground	Carried fuel mass	100 kg	Air/ground
Equivalent active area S_c	12.5 m^2	Air	Number of ducted fans/wheels	4	Air/ground
Mass conversion factor δ	1	Ground	Air density ρ	1.22 kg/m^3	Air/ground

2.1. Turbine Generation System

The turbine generation system consists of a turboshaft engine and a generator, which are connected by a mechanical shaft or integrated design. In this paper, the subsystem modeling of the turboshaft engine and generator is developed by the analytical method.

2.1.1. Turboshaft Engine

The turboshaft engine is mainly composed of the compressors, combustion chamber, recuperator, core turbine, and power turbine [51], and its detailed system configurations and connections can be seen in Figure 2. Low-pressure compressor with inlet guide vanes and centrifugal high-pressure compressor can compress inlet airflow and control airflow through the bleed-off valve. A mixture of fuel and air is ignited in the combustion chamber, producing gas that powers the core turbine. Then, the core turbine drives two compressors in a mechanical connection to balance the load and stabilize the speed. The power turbine shaft output port is connected to the generator to output mechanical energy.

The component characteristics of a turboshaft engine emphasize its parameters such as output power, operation temperature, fuel consumption, and exhaust emissions. It is assumed that the air is composed of oxygen (O_2), nitrogen (N_2), and argon (Ar), and three groups of species in the combustion chamber are considered: hydrocarbon or fuel ($C_{10}H_{20}$), air (O_2, N_2, Ar), and burned gases (CO_2, H_2O, N_2).

$$C_{10}H_{20} + 15(O_2 + \frac{x_{N_2}}{x_{O_2}}N_2) \longrightarrow 10CO_2 + 10H_2O + 15\frac{x_{N_2}}{x_{O_2}}N_2. \tag{1}$$

Therefore, the CO_2 emissions from the combustion chamber can be calculated from the consumption of hydrocarbon fuels, which serves as an indicator for evaluating the emission performance of the TEHPS. Furthermore, the power of compressors and turbines can be calculated from their rotational speed ω and torque T according to the rotating mechanical characteristics.

$$\begin{aligned} P_{comp} &= \omega_{comp} \cdot T_{comp} = \dot{m}_{reac}[h(p_{out}, t_{out}) - h(p_{in}, t_{in})] \\ P_{turb} &= \omega_{turb} \cdot T_{turb} = \dot{m}_{reac}[h(p'_{in}, t'_{in}) - h(p'_{out}, t'_{out})], \end{aligned} \tag{2}$$

where $\dot{m}_{reac}$ is the fuel chemical reaction rate occurring in the combustor, p_{out}, t_{out} and p_{in}, t_{in} are the outlet or inlet pressure and temperature, and $h(p, t)$ represent the specific enthalpy of the compressors or turbines.

The turboshaft engine incorporates several temperature control components such as the compressors, turbines, and combustion chamber, and its temperature limits for the turbine entry, exhaust gas, and compressor discharge are given as 640 K, 1035 K, and 1400 K, respectively. In addition, the nominal power of the turboshaft engine is 420 kW, and its current fuel mass flow rate $\dot{m}_{fuel,cur}$ (kg/s) can be calculated according to the real-time output power P_{eng} (kW), evaluating the overall fuel consumption of the TEHPS [17,52].

$$\dot{m}_{fuel,cur} = -6.98 \times 10^{-9} * P_{eng}^2 + 6.76 \times 10^{-5} * P_{eng} + 7.89 \times 10^{-3}. \tag{3}$$

2.1.2. Generator

Generator models are inclined to characterize the energetic behavior occurring within the component, where the generator is connected to the front-end turboshaft engine by a mechanical shaft and converts the mechanical energy into electrical energy. The internal model and external control circuit of the generator are shown in Figure 3. The reference speed of the turboshaft engine output shaft forms a deviation signal with its actual speed, which is converted into the maximum current instruction ratio *Sig* of the generator by the PI controller. Then the control signal obtains the generator output current coefficient C_g

through the limiting link and filtering link. Hence, the output current and power of the generator can be computed.

$$\begin{aligned} I_{gen} &= C_g \cdot I_{gen,max} \\ P_{gen} &= U_{gen} \cdot I_{gen}, \end{aligned} \tag{4}$$

where $I_{gen,max}$ represent the maximum permissible current for generator operation.

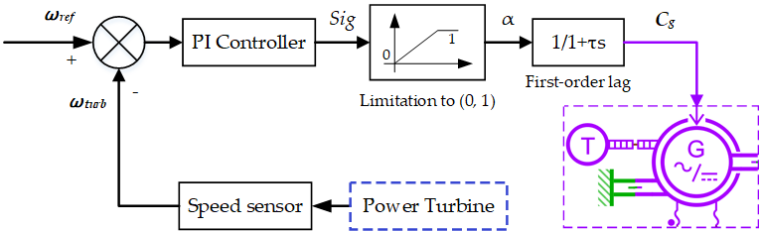

Figure 3. Generator model and its external control diagram.

2.2. Hybrid Energy Storage System

A hybrid energy storage system consists of energy-based and power-based energy storage mediums, and the comparison of power and energy density of various energy storage devices can be drawn from reference [53]. Lithium battery can respond to the short time low amplitude power demand of the load with higher output energy, and supercapacitor typically reacts to the instantaneous peak power demand with less relative energy. As shown in Figure 4, the HESS mainly includes a lithium battery pack, supercapacitor pack, and bi-directional DC/DC converters. The energy storage units are connected in parallel to the DC bus, which increases the system capacity and enables the regulation of the bus voltage and system power. The battery and supercapacitor pack consists of several cells connected in series and parallel with the individual parameters shown in Table 2.

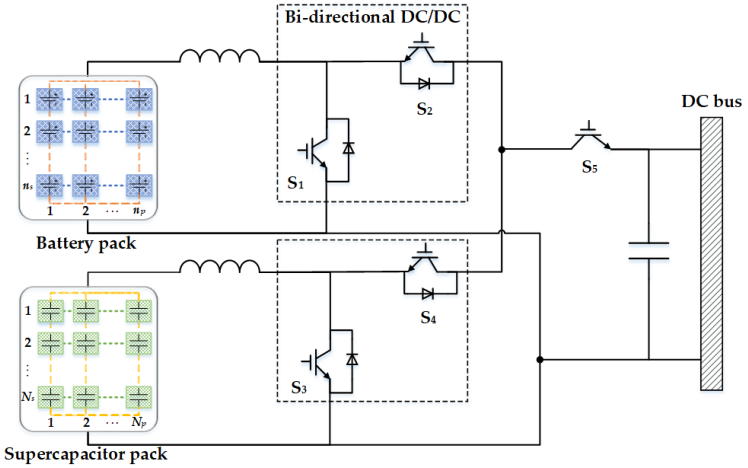

Figure 4. Configuration of the battery pack, supercapacitor pack, and bi-directional DC/DCs in the hybrid energy storage system.

Table 2. Basic parameters of battery and supercapacitor.

Type	Title	Value	Unit	Type	Title	Value	Unit
Battery	Rated capacity	2.3	Ah	Supercapacitor	Rated capacity	450	F
	Cell mass	0.07	kg		Cell mass	0.018	kg
	Material density	2028	kg/m^3		Material density	1768	kg/m^3
	Thermal conductivity	1.5	W/m/K		Thermal conductivity	15	W/m/K
	Voltage range	[2, 3.6]	V		Nominal voltage	3.8	V
	Temperature range	[−30, 60]	degC		Temperature range	[−30, 60]	degC

2.2.1. Battery Pack

Lithium batteries are the primary choice for energy storage in the TEHPS due to their higher energy density, greater charge or discharge ratio, and longer lifetime. The battery pack consists of several identical cells connected in series or parallel, where the number is determined by the pack power, total capacity, and reference voltage. What is more, the battery cell adopts the quasi-static equivalent circuit model, which not only captures the non-linear electrochemical phenomena but also avoids the tedious calculation of electrochemical processes.

The battery pack's open circuit voltage and resistance can be calculated from the following equations.

$$\begin{aligned} V_{oc}(SOC_b, T) &= n_s \cdot V_{cell}(SOC_b, T) \\ R_{in}(SOC_b, T) &= \frac{n_s}{n_p} \cdot R_{cell}(SOC_b, T), \end{aligned} \tag{5}$$

where V_{cell} and R_{cell} are the function of the state of charge SOC_b and working temperature T and represent the open circuit voltage and internal resistance of the battery cell. n_s and n_p denote the number of series and parallel connections in the battery pack. Based on Kirchhoff's current–voltage law, the output voltage of the battery pack can be calculated as:

$$U_{bat} = V_{oc} - I_{bat} \cdot R_{in}. \tag{6}$$

In conjunction with Ohm's law $P_{bat} = U_{bat} \cdot I_{bat}$, the above equation can be combined to obtain the expression for the battery output current as:

$$I_{bat} = \frac{V_{oc} - \sqrt{V_{oc}^2 - 4P_{bat} \cdot R_{in}}}{2R_{in}}. \tag{7}$$

Moreover, the battery's SOC_b can be determined from the current, capacity Q_{bat} and its charge or discharge efficiency η, and the final expression is shown below.

$$SOC_b = \frac{1}{\eta^{sign(I_{bat})}} \frac{V_{oc} - \sqrt{V_{oc}^2 - 4P_{bat} \cdot R_{in}}}{2R_{in} \cdot Q_{bat}}. \tag{8}$$

In order to verify the validity of the battery cell model, virtual experimental tests based on the software Simceter AMEsim are implemented. The 2.3 Ah battery cell is carried out on a virtual test bench at 20 °C using a specific input current pattern, started at full state of charge (SOC_b = 100%) and continuously discharged with a current of 2.3 A for 400–2200 s. Then the battery cell is at rest with no current flowing until 4000 s, and the last 2000 s is spent in continuous transient charge or discharge operation to simulate the practical working conditions. As shown in Figure 5, the results show that the quasi-static model can predict the battery voltage well during the continuous discharge and rest phases of the battery, with an uncertainty of less than 1 °C in the temperature prediction. During the non-constant charge or discharge phase, the model voltage has some acceptable uncertainty (<50 mV) and the overall trend of the battery SOC_b is consistent with the initial design value.

2.2.2. Supercapacitor Pack

A supercapacitor is an energy storage system that stores energy electrostatically in the electrochemical double layer at electrodes and electrolyte interfaces providing the high capability of current absorption and release [54]. In addition, supercapacitors can be used in combination with batteries to absorb or supply high power requirements, both to prevent high current battery aging and to mitigate high heat losses within the battery pack. Similarly, supercapacitor modeling adopts the simplified electrical equivalent circuit approach only taking into account the main capacitance, internal resistance, and electrical leakage.

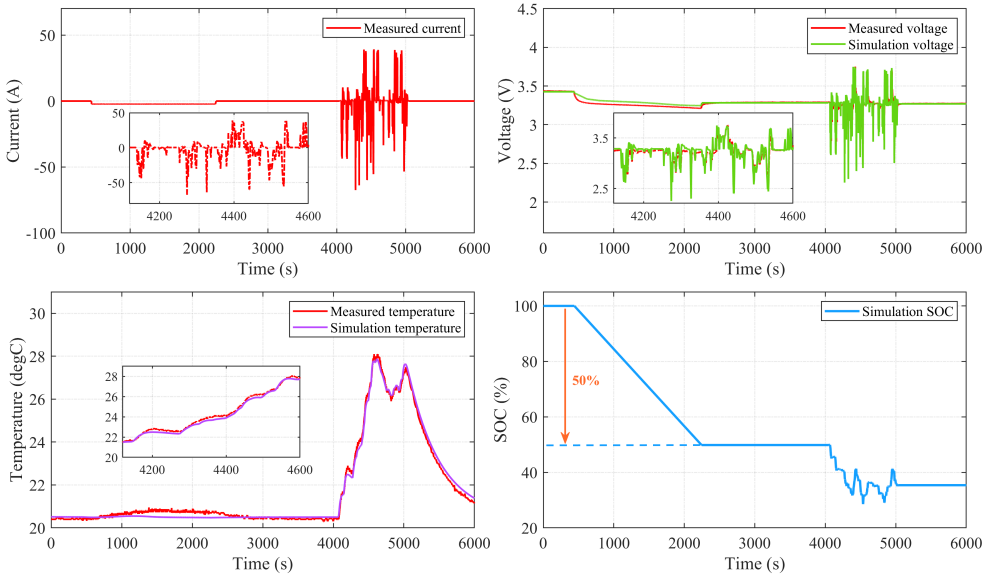

Figure 5. Test measurement and simulation results of 2.3 Ah battery cell (current, voltage, temperature, and SOC).

The current and voltage relationship between the supercapacitor cell and pack are expressed as:

$$\begin{aligned} I_{sc} &= I_{cell} \cdot N_p \\ U_{sc} &= U_{cell} \cdot N_s, \end{aligned} \tag{9}$$

where N_s and N_p denote the number of series and parallel connections. The internal resistance voltage and leakage voltage of the supercapacitor cell can be solved with the differential equation.

$$\begin{aligned} \frac{dU_{R_{in}}}{dt} &= \frac{dU_{cell}}{dt} - \frac{1}{C_{nom}} \cdot \left(\frac{U_{R_{in}}}{R_{in}} - \frac{U_{R_{leak}}}{R_{leak}}\right) \\ U_{R_{leak}} &= U_{cell} - U_{R_{in}}, \end{aligned} \tag{10}$$

where C_{nom} and R_{in} represent the nominal capacitance and internal resistance, respectively. In particular, the supercapacitor pack state of charge SOC_{sc} is defined as the ratio of stored energy $E(t)$ over the maximum energy E_{max} that can be stored at the maximum voltage U_{max} according to:

$$\frac{SOC_{sc}}{100} = \frac{E(t)}{E_{max}} = \frac{U(t)^2}{U_{max}^2}. \tag{11}$$

2.2.3. Bi-Directional DC/DC Converters

In order to achieve a better energy distribution between the battery and supercapacitor and improve HESS efficiency, a bi-directional full-bridge isolated topology is chosen for the DC/DC converter. Dual quadrant operation is achieved by changing the current direction according to actual requirements while maintaining the polarity of the input and output voltages. The discharge or charge operating state of the battery and supercapacitor should be taken into account when performing power calculations. For each of these DC/DC converter types, there are a switched and an average model, and both of them estimate semiconductor losses. In this paper, setting the bi-directional converter efficiency to a

constant value η_{conv}, the losses incurred during charging and discharging are shown in the following equation.

$$l_{conv} = \begin{cases} P_{bat/sc} \cdot (\frac{1}{\eta_{conv}} - 1), P_{bat/sc} \geq 0 \\ -P_{bat/sc} \cdot (1 - \eta_{conv}), P_{bat/sc} < 0, \end{cases} \quad (12)$$

where $P_{bat/sc}$ is the power of the battery or supercapacitors pack, with a positive sign indicating discharge and a negative sign indicating a charge.

2.3. Distributed Electric Drive-Propulsion System

The distributed electric drive-propulsion system (DEDPS) is composed of distributed electric motors, a ground drive unit, and an air propulsion device. According to the different flight conditions and missions of HAGA, the integrated controller can dynamically adjust the load port.

2.3.1. Drive Units

Obviously, the drive units in the DEHPS have mainly four hub motors and four rotor motors. Brushless direct current motors are suitable for application in hybrid propulsion due to their small size, light weight, high power density, and wide speed regulation range. The control principle of the distributed electric drive-propulsion system is shown in Figure 6, where the parallel distributed arrangement of BLDC sets (M_{r1-r4} and M_{h1-h4}) serves as the main drive source, driving the wheels on the ground and ducted fans in the air.

After determining the DC bus voltage, the current input to the distributed motors is dynamically allocated to the power generation system and HESS side according to the effective energy management strategy. The motor control unit (MCU) in the DEDPS takes the voltage limit value, torque, and speed signals as input. The MCU can output the current signal through PI regulation, coordinate transformation, and space vector pulse width modulation to achieve effective torque control.

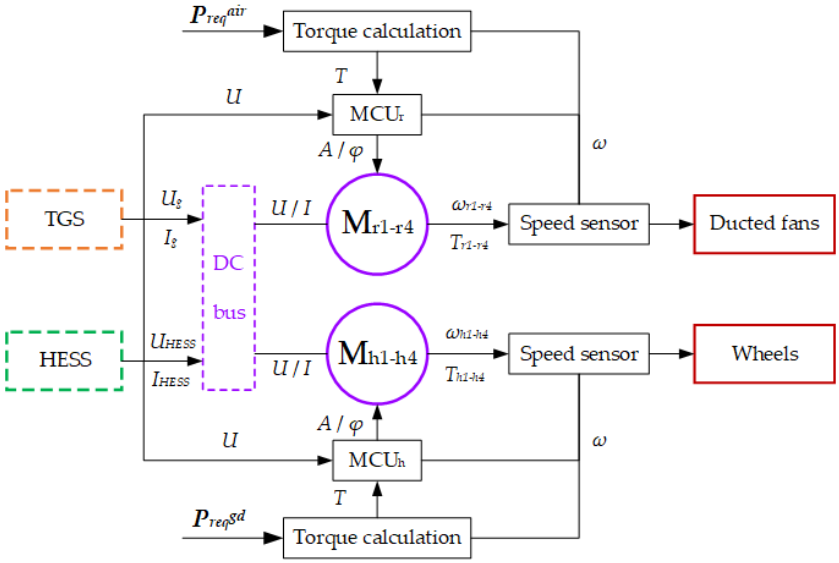

Figure 6. Configuration of distributed electric drive-propulsion units.

2.3.2. Propulsion Units

The propulsion units are the wheels which generate the horizontal thrust force, and the ducted fans, which provide the vertical lift for HAGA. The air drive and propulsion units are treated as a constant load when the air–ground aircraft is traveling on the ground. Only longitudinal dynamics are considered, and four kinds of rolling resistance F_{roll}, air

drag F_{air}, ramp resistance F_{ramp}, and acceleration resistance F_{acc} generated by external environment and vehicles themselves need to be overcome.

$$F_{drive} = \underbrace{M_T g C_r cos\beta}_{F_{roll}} + \underbrace{\frac{1}{2}\rho S C_{ad} V_g^2}_{F_{air}} + \underbrace{M_T g sin\beta}_{F_{ramp}} + \underbrace{\delta M_T \frac{dV_g}{dt}}_{F_{acc}}, \tag{13}$$

where M_T refers to the total mass, g is the gravity acceleration, C_r and C_w represent the roll resistance and wind resistance coefficient, β is the road slope, S is the aircraft active area, V_g denotes the ground speed of the HAGA, and δ is the rotating mass conversion factor, which converts the inertia moment of the rotating mass into that of the translational mass.

Ducted fans allow the analog conversion of shaft power to aerodynamic power with the input parameters air density, flight speed V_{air}, wind speed V_{wind}, and blade pitch angle, its module diagram and working principle can be seen from Figure 7. The aerodynamic velocity is a function of the aircraft speed and the wind speed, both of them relative to the Earth.

$$V_{aero} = V_{air} - V_{wind}, \tag{14}$$

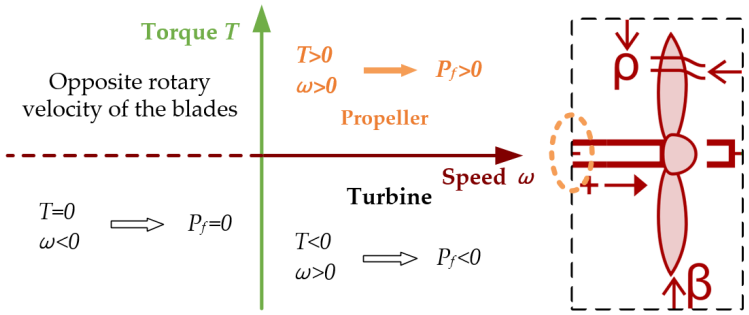

Figure 7. Schematic diagram of ducted fans module and its working principle.

The thrust F_f and torque T_f of ducted fans are calculated according to the thrust coefficient C_T and power coefficient C_P, and the blade profile is selected as NACA0016 [55].

$$\begin{aligned} F_f &= C_T \cdot \rho \cdot \Omega_f^2 \cdot d^4 \\ T_f &= C_P \cdot \rho \cdot \Omega_f^3 \cdot d^5 / \omega_f, \end{aligned} \tag{15}$$

where d is the blade diameter, Ω_f is the angular speed (rev/s), ω_f and is the angular speed in SI units (rad/s). It should be noted that C_T and C_P can be calculated from the blade element-momentum theory, which is expressed as the one-dimensional quadratic function of the advance ratio J [56]. The equation coefficients are determined by pitch δ_f, mean chord length $\overline{C_b}$, diameter d, and number of blades n_b.

Eventually, the operating characteristics of ducted fans are assessed from their aerodynamic efficiency and the expression is:

$$\begin{aligned} \eta_f &= J \cdot \frac{C_T}{C_P} \\ J &= \frac{V_{aero}}{\Omega_f \cdot d}. \end{aligned} \tag{16}$$

3. Description for Turbo-Electric Hybrid Propulsion System

System-level and component-level power analysis, energy analysis, and weight analysis in the different phases are carried out for the TEHPS model to provide a theoretical basis for powertrain size optimization and energy management.

3.1. Power Analysis

3.1.1. Power Requirement Analysis

The power analysis should be carried out according to the dynamic characteristics of the air flight or ground drive modes, where the air flight is divided into VTOL and cruise flight modes. Ducted fans can provide lift to the HAGA during the VTOL phase, and the lift force F_{vtol} is equal to the sum of the gravity, acceleration resistance, and flat plate drag D_{air}, which neglects the vertical aerodynamic force acting on the center body. Therefore, the required power can be expressed as [57,58]:

$$\begin{aligned} P_{req}^{air,vtol} &= \frac{F_{vtol} \cdot V_f}{\eta_{rot}} \\ F_{vtol} &= M_T g + (\delta M_T a_v + D_{air}) \cdot sign(V_{air}) \\ V_f &= -\frac{R_{climb}}{2} + \sqrt{\frac{R_{climb}^2}{4} + \frac{F_{vtol}}{2 \cdot \rho \cdot S_f}} \\ D_{air} &= \rho \cdot R_{climb}^2 \cdot S_f \cdot sin^3 \alpha \\ sign(V_{air}) &= \begin{cases} 1, climb \\ -1, land, \end{cases} \end{aligned} \tag{17}$$

where V_f is the axial induced velocity through the rotor disc, η_{rot} is the rotor utility factor R_{climb} is the rate of climb, α represents the angle of attack, and S_f represents the rotor disc area which can be calculated from blades diameter and number.

In the cruise flight phase, the lift force is equal to gravity, and drag force is equal to thrust, so the required power can be calculated as follows:

$$\begin{aligned} P_{req}^{air,cruise} &= F_{cruise} \cdot V_{cruise} \\ F_{cruise} &= \sqrt{F_h^2 + F_{vtol}^2} \\ F_h &= \delta M_T a_h + \frac{1}{2} \rho S_c C_w V_h^2, \end{aligned} \tag{18}$$

where V_{cruise} and V_h denote the cruise and horizontal flight speed, F_h is the horizontal force, a_h is the horizontal acceleration speed, and S_c is the equivalent active area in cruise.

Moreover, the power when the HAGA is driving on the road can be expressed as:

$$P_{req}^{gd} = F_{drive} \cdot V_g = (M_T g C_r cos\beta + \frac{1}{2} \rho S C_{ad} V_g^2 + M_T g sin\beta + \delta M_T \frac{dV_g}{dt}) \cdot V_g, \tag{19}$$

where V_g is the ground traveling speed. Finally, the maximum power value of the TEHPS parameter design is determined by comparing the required power under different flight conditions.

$$P_{req} = max\left\{ P_{req}^{air,vtol}, P_{req}^{air,cruise}, P_{req}^{gd} \right\}. \tag{20}$$

3.1.2. Power Supply-Side and Demand-Side Analysis

The existence of a hybrid energy storage system brings a new degree of freedom to the power flow in the TEHPS, and the power supply and demand sides of HAGA should be dynamically balanced during the entire mission profile.

$$P_{TGS} + P_{HESS} = P_{ADEPS} \cdot f_{air} + P_{GDEDS} \cdot (1 - f_{air}), \tag{21}$$

where f_{air} is the flag that the HAGA is in flight and f_{air} = 0 when travelling on the ground. In the drive state, the turbine generation system and hybrid energy storage system are

acting as power sources simultaneously for the supply side when the required power is high.

$$\begin{aligned} P_{TGS} &= P_{eng} \cdot \eta_{gen} \cdot \eta_{rect} \\ P_{HESS} &= P_{bat} \cdot \eta_{conv} + P_{sc} \cdot \eta_{conv}. \end{aligned} \tag{22}$$

where η_{rect} is the efficiency of AC/DC rectifier, P_{HESS} represents the power of hybrid energy storage system.

For the demand side, the air-distributed electric propulsion system (ADEPS) and ground-distributed electric drive system (GDEDS) consume power as loads.

$$\begin{aligned} P_{ADEPS} &= n_{rm} \cdot P_{rm} \\ P_{GDEDS} &= n_{hm} \cdot P_{hm} \end{aligned} \tag{23}$$

where n_{rm} and n_{hm} represent the number of rotor motors and hub motors. When the required power is less than the generator side output power and the SOC of the battery in HESS is less than the initial value of 0.8, the turbine generation system adjusts the engine operating point to both power the distributed electric propulsion system and charge the remaining power to the HESS, at which $P_{HESS} < 0$.

3.2. Energy Analysis

The energy provided by the power and energy sources is necessary to cover the HAGA energy requirements for a given air flight and ground travel cycle, so the overall energy requirements can be calculated as:

$$E_{req} = \underbrace{\int_0^{t_{air,vtol}} P_{req}^{air,vtol} dt}_{E_{air,vtol}} + \underbrace{\int_0^{t_{air,cruise}} P_{req}^{air,cruise} dt}_{E_{air,cruise}} + \underbrace{\int_0^{t_{gd}} P_{req}^{gd} dt}_{E_{gd}}, \tag{24}$$

where $t_{air,vtol}$, $t_{air,cruise}$, and t_{gd} represent the VTOL phase, cruise phase, and ground travel time, respectively. There are various forms of energy conversion in the TEHPS such as fuel internal energy, electrical energy, and mechanical energy, and the production, loss, and consumption of energy follow the energy conservation law. Therefore, the electric energy balance equation can be expressed as:

$$E_{rm} + E_{hm} = E_{gen} + E_{bat} + E_{sc}, \tag{25}$$

where $E_{rm/hm}$, E_{gen}, E_{bat}, and E_{sc} indicate the electrical energy demanded by the rotor and hub motors, supplied by the generator, battery, and supercapacitor, respectively.

3.3. Weight Analysis

The weight of hybrid air–ground aircraft is closely associated with the system power and energy requirements, and the total weight M_T can be computed with:

$$\begin{aligned} M_T &= M_{st} + M_{TEHPS} + M_{load} \\ M_{st} &= k_{st} \cdot M_T, \end{aligned} \tag{26}$$

where M_{st} is the structure mass, k_{st} is the structural mass coefficient, M_{load} represents the load mass and its value is determined according to the design requirements, and M_{TEHPS} refers to the total mass of turbo-electric hybrid propulsion system including multiple subsystem parts.

$$\begin{aligned} M_{TEHPS} = \underbrace{M_{eng} + M_{fuel} + M_{gen} + M_{rect}}_{M_{TGS}} + \underbrace{M_{bat} + M_{sc} + M_{conv}}_{M_{HESS}} \\ + \underbrace{n_{rm} \cdot (M_{rm} + M_{fan})}_{M_{ADEPS}} + \underbrace{n_{hm} \cdot (M_{hm} + M_{wh})}_{M_{GDEDS}}, \end{aligned} \tag{27}$$

where M_{TGS} involves the components mass of turboshaft engine M_{eng}, fuel M_{fuel}, generator M_{gen}, and power electronics M_{rect} specifically, and can be expressed as:

$$\begin{aligned} M_{eng} = P_{eng}/\xi_{eng}, M_{fuel} = \int_0^{t_{eng}} \dot{m}_{fuel,cur}(P_{eng})dt \\ M_{gen} = P_{gen}/\xi_{gen}, M_{rect} = P_{rect}/\xi_{rect}, \end{aligned} \tag{28}$$

where ξ_{eng}, ξ_{gen}, and ξ_{rect} are the power density of the turboshaft engine, generator, and AC/DC rectifier, and t_{eng} indicates the operating time of turboshaft engine. In addition, the total mass of the battery and supercapacitor pack is obtained from the product of the number of series and parallel branches and the cell unit mass.

$$\begin{aligned} M_{bat} &= n_{bat} \cdot m_{bat,cell} = n_s \cdot n_p \cdot m_{bat,cell} \\ M_{sc} &= N_{sc} \cdot m_{sc,cell} = N_s \cdot N_p \cdot m_{sc,cell} \\ M_{conv} &= \sum P_{conv}/\xi_{conv}, \end{aligned} \tag{29}$$

where n_{bat} and N_{sc} denote the total number of battery and supercapacitor cells, and ξ_{conv} is the power density of DC/DC converters.

Moreover, the mass of electric motors in the electric drive-propulsion system is determined by an empirical formula and the ducted fan mass is dictated by the blade material and its geometric characteristics.

$$\begin{aligned} M_{em} &= n_{rm} \cdot P_{rm}/\xi_{rm} + n_{hm} \cdot P_{hm}/\xi_{hm} \\ M_{fan} &= \frac{n_{rm} n_b d^2 \overline{C_b} \sigma_b}{4}, M_{wh} = n_{hm} \cdot m_{wh}, \end{aligned} \tag{30}$$

where σ_b are the number, mean chord, and average density of the blades, and m_{wh} indicates the wheel mass which is set as a constant.

4. Size Optimization and Energy Management for TEHPS

In order to minimize the fuel and emission costs and maximize the energy conversion efficiency of the turbo-electric hybrid propulsion system in the HAGA, a size optimization method based on the genetic algorithm and a hierarchical energy management framework based on the equivalent consumption minimization strategy and fuzzy logic control are proposed in this section.

4.1. Sizing Optimization Method

The power, energy, and mass analysis of TEHPS demonstrate that there exists a functional relationship between the components' mass and the total power and energy. Therefore, a set of design parameters should be obtained that minimizes HAGA mass and maximizes system efficiency while meeting the power and energy requirements. The principle of TEHPS parameters design and optimization is shown in Figure 8. The optimization parameters of the genetic algorithm were set as population size PS = 20, crossover rate CR = 0.95, mutation rate MR = 0.05, and number of generations G_{max} = 200.

On the one hand, taking the minimum total mass M_T as the design objective, the equality constraint is expressed as the balance of each component's mass. Additionally, the inequality constraint is expressed as the number of energy storage units calculated from the maximum power and energy demand is not greater than the design number.

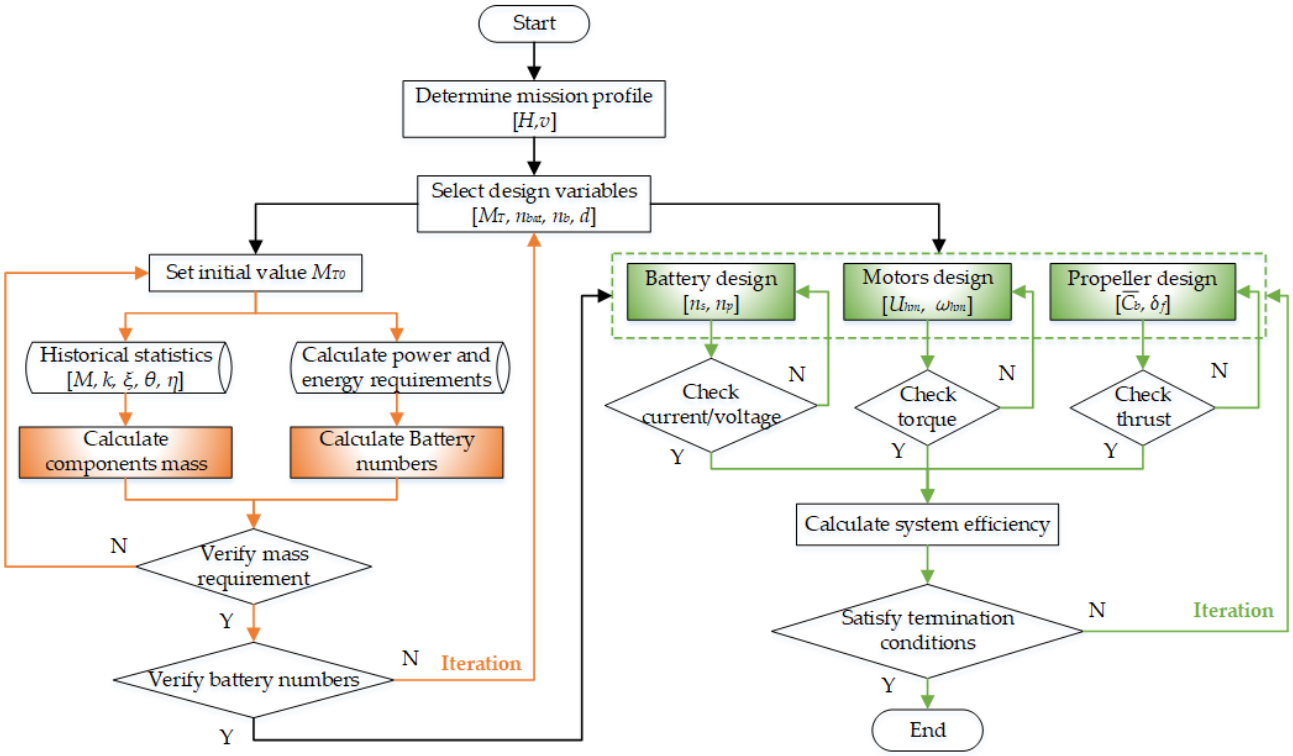

Figure 8. Sizing methodology schematic of the TEHPS.

$$\min_{x_i} J = M_T$$
$$s.t. \begin{cases} (1-k_{st})M_T = n_{bat}m_{bat,cell} + N_{SC}m_{sc,cell} + M_{load} + M_{TGS} + M_{em} + M_{fan} + M_{wh} \\ max\left\{P_{req}^{air,vtol}, P_{req}^{air,cruise}, P_{req}^{gd}\right\} - (P_{TGS} + n_{bat}m_{bat,cell}\xi_{bat}\eta_{conv} + N_{SC}m_{sc,cell}\xi_{sc}\eta_{conv}) \le 0 \\ (E_{air,vtol} + E_{air,cruise} + E_{gd}) - (E_{gen}\eta_{rect} + n_{bat}m_{bat,cell}\theta_{bat} + N_{SC}m_{sc,cell}\theta_{sc}) \le 0. \end{cases} \quad (31)$$

Firstly, the mission profile height and speed are determined and design variables $[M_T, n_{bat}, N_{SC}, n_b, d]$ are selected. The initial weight is set to M_{T0} and the various components' masses are calculated based on the historical information, as indicated in Table 3. At the same time, the number of batteries and supercapacitors is calculated based on the overall power and energy requirements. The initial weight is then updated and iterated until the energy demand matches the equation constraint. Finally, the design variables are adapted to satisfy each inequality constraint to complete the static parameters optimization.

Table 3. Historical statistics of components' parameters.

Title	Value	Unit	Title	Value	Unit
Turboshaft engine power density	3	kW/kg	Load mass	200	kg
Battery cell mass	0.07	kg	Generator power density	3	kW/kg
Battery energy density θ_{bat}	180	Wh/kg	Rotor/hub motor power density	3	kW/kg
Battery power density ξ_{bat}	1000	W/kg	Wheel mass	10/15	kg
Supercapacitor cell mass	0.018	kg	Rectifier/converter efficiency	0.95	-
Supercapacitor energy density θ_{sc}	8.55	Wh/kg	Rectifier/converter power density	8	kW/kg
Supercapacitor power density ξ_{sc}	3000	W/kg	Structural mass coefficient	0.4	-

On the other hand, HAGA have long operating times and high energy requirements during the cruise flight phase, so further improvements to the ADEPS are required to improve the energy conversion efficiency. The second optimization objective is the electric propulsion efficiency and design variables are selected as $[n_s, N_s, U_{rm}, \omega_{rm}, \overline{C_b}, \delta_f]$. Several inequality constraints should be fulfilled: the available thrust of ducted fans is not less than

the demand thrust, the available torque of rotor motors is not less than the demand torque of ducted fans, the voltage level of the HESS is not less than the motors input voltage, and the current provided by the generator, batteries, and supercapacitors is not less than the motor operating current.

$$\max_{x_i} J = \frac{T_{rm}\omega_{rm}}{U_{rm}I_{rm}} \cdot \frac{F_f V_{cruise}}{T_f \Omega_f}$$
$$s.t. \begin{cases} \sqrt{F_h^2 + F_{vtol}^2} - n_f \cdot \rho d^4 \Omega_f^2 C_T \le 0 \\ \rho d^5 \Omega_f^3 C_P - k_T \cdot \frac{U_{rm} - k_E \omega_{rm}}{r_{rm}} \le 0 \\ U_{rm} - min\{n_s U_{bat,cell}, N_s U_{sc,cell}\} \le 0 \\ n_{rm} I_{rm} - [(n_p I_{bat,cell} + N_p I_{sc,cell}) + I_{gen}] \le 0 \\ n_s n_p - n_{bat} = 0 \\ N_s N_p - N_{sc} = 0. \end{cases} \quad (32)$$

For the ducted fans, the pitch δ_f and mean chord length $\overline{C_b}$ are initially selected as design variables, and the thrust and torque coefficients are calculated based on the previous equations. According to the rotor motor power level, different types are selected to determine the back electromotive force constant k_E and torque constant k_T, and the output torque is calculated. At last, the output voltage and current of the HESS are calculated based on the number of batteries and supercapacitors. Parameter optimization will be completed once the calibrations of the ducted fans thrust, motors torque, HESS voltage, and current have been completed and the set system efficiency thresholds have been reached.

The genetic algorithm is adopted for the multi-objective optimization of the HAGA sizing methodology to solve for component parameters in the TEHPS that match the power, energy, and efficiency requirements. An approximate global optimum solution is considered to be obtained when the genetic algorithm terminates. In this paper, the maximum fitness value or average fitness value tends to stabilize as the termination condition within the maximum number of iterations. The simulation results indicate that in the first optimization, when the number of iteration steps is 22, the fitness value tends to be stable and the approximate optimal solution is obtained. In the second optimization, the optimization stops to obtain the optimal solution when the number of iteration steps is 50. Finally, the sizing design results obtained from the iterations are shown in Table 4.

Table 4. Optimization results of sizing design.

Title	Value	Title	Value
Total mass	2100 kg	Supercapacitor number	2321
Blade number	3	Supercapacitor series number	211
Ducted fans diameter	1.5 m	Supercapacitor parallel number	11
Battery number	1250	Rotor motor speed	3200 rpm
Battery series number	250	Motor voltage	800 V
Battery parallel number	5	Mean chord length	0.1125 m

4.2. Energy Management Framework

An energy management framework for the TEHPS is proposed in this section, which performs energy management and power allocation from both the upper system level and lower component level. The algorithm flow chart of the hierarchical energy management strategy is shown in Figure 9.

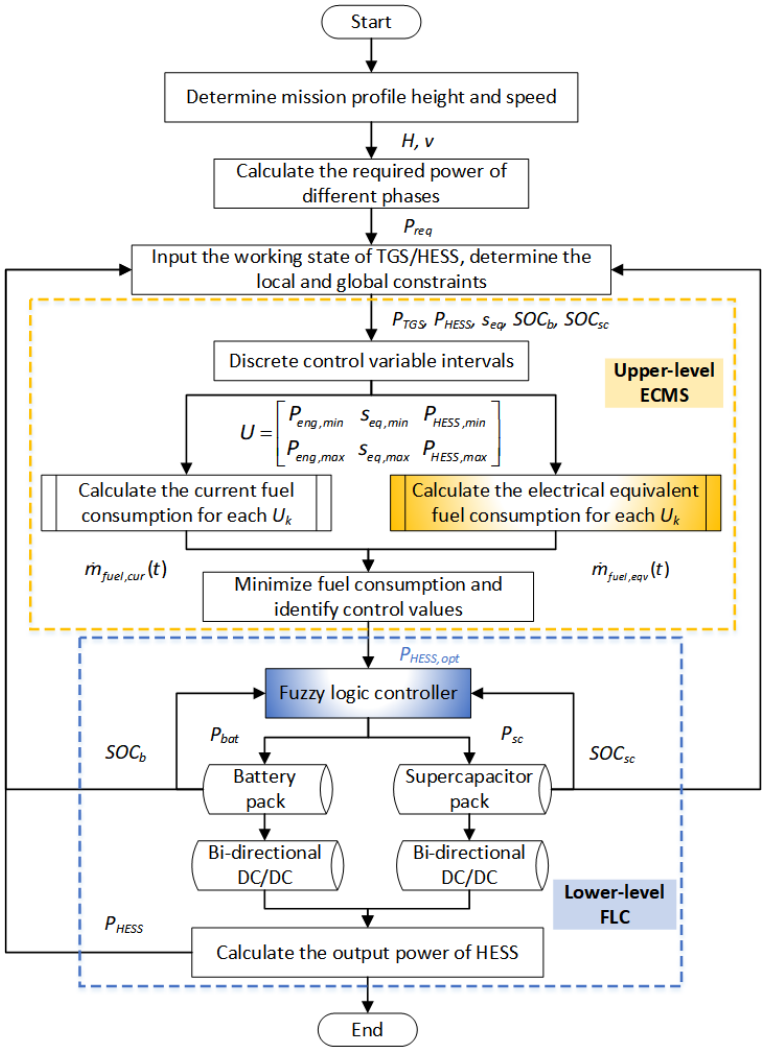

Figure 9. Hierarchical energy management framework of the TEHPS.

4.2.1. Upper-Level Energy Management

The upper-level energy management controller applies the equivalent fuel consumption minimization strategy to dynamically distribute the power output of the turbine power system and hybrid energy storage system. The overall system performance evaluation function can be expressed as:

$$\begin{aligned} minJ &= \int_{t_0}^{t_f} \dot{m}_{fuel}(x(t), u(t), t)dt \\ x(t) = [SOC_b(t), SOC_{sc}(t)], u(t) &= [P_{eng}(t), s_{eq}(t), P_{HESS}(t)], \end{aligned} \tag{33}$$

where t_0 and t_f indicate the start time and end time of the flight mission, and $x(t)$ and $u(t)$ represent the state variables and control variables. The integrated energy management controller is optimized for total fuel consumption, and ECMS can establish an equivalent relationship between the electricity spent in the HESS and the fuel consumption in the TGS.

$$\dot{m}_{fuel}(t) = \dot{m}_{fuel,cur}(t) + \dot{m}_{fuel,eqv}(t), \tag{34}$$

where $\dot{m}_{fuel,cur}(t)$ and $\dot{m}_{fuel,eqv}(t)$ denote the current fuel consumption and equivalent fuel consumption, respectively, obtained by converting electrical power usage of the HESS.

$$\dot{m}_{fuel,eqv}(t) = s_{eq}(t) \cdot \frac{P_{HESS}(t)}{Q_{fuel,low}}, \tag{35}$$

where $s_{eq}(t)$ represents the equivalent factor, and $Q_{fuel,low}$ is the low calorific value of aviation fuel, which is the available energy contained per unit mass of fuel, $Q_{fuel,low}$ = 48,140 KJ/kg.

Inherently, the ECMS is a heuristic for optimal control and is equivalent to Pontryagin's minimum principle (PMP) [59], computed by solving two-point side problems for differential or difference equations derived from PMP, discretizing control variables and establishing equations and inequality relationships based on state space analysis. The equivalence factor denotes the efficiency chain in the interconversion of fuel and electricity, which varies with the operating conditions of the TEHPS. Regardless of charging and discharging losses, the equivalence factor s_{eq} can be taken equivalently to the co-variable λ in the PMP. Set the range of $s_{eq} \in [2, 4.5]$ according to the simulation experience, and initially s_{eq_0} = 3. The bisection method is applied to iterate continuously, and the value is determined according to the relationship between the equivalence factor and SOC difference and fuel consumption. In addition, the bisection method converges at s_{eq} = 3.6, taking this value as the constant value for the subsequent cycle.

Specifically, the powertrain state parameters and constraint ranges are first imported and the control interval is discretized. For each control vector, the current fuel consumption and equivalent fuel consumption are calculated, and the P_{HESS} that minimizes the total fuel consumption is picked, thus completing the design and calculation of the local ECMS optimization.

4.2.2. Lower-Level Energy Management

Lower-level energy management is embodied in the component-level power split strategy for hybrid energy storage systems. Batteries have excellent energy characteristics but can be limited by their power characteristics, whereas a supercapacitor can provide high power in a short time period. Therefore, during the VTOL phases of HAGA, the high-frequency component of required power can be handled by a supercapacitor pack, reducing the impact of high current discharge on the battery and extending its life cycle.

Fuzzy logic control is highly robust when measuring imprecise dynamic characteristics and is, therefore, useful for distributing the output power of the individual energy storage units. The HESS power P_{HESS}, the state of charge of battery pack SOC_b and supercapacitor pack SOC_{sc} are set as fuzzy input variables, while the power split factor f_p is given as a fuzzy output variable.

$$\begin{aligned} P_{HESS}(t) &= P_{bat}(t) \cdot \eta_{conv} + P_{sc}(t) \cdot \eta_{conv} \\ P_{bat}(t) = P_{HESS}(t) \cdot f_p, P_{sc}(t) &= P_{HESS}(t) \cdot (1 - f_p). \end{aligned} \tag{36}$$

A fuzzy logic controller involves determining the variable domain, identifying the variable membership function, and designing fuzzy rules. In order to improve the control accuracy, the affiliation function of four fuzzy variables is combined with some non-uniformly distributed functions including generalized bell-shaped, Gaussian-type, and Z/S-shaped, and the input/output affiliation functions are shown in Figure 10. For the three-input one-output controller, the input variable fuzzy domain of the HESS power P_{HESS} is [0, 1], and its fuzzy subset is {VS, S, M, L, VL}; the battery SOC_b and supercapacitor SOC_{sc} both have a fuzzy domain of [0, 100] and a fuzzy subset of {S, M, L}. Furthermore, the fuzzy domain of the output variable f_p is [0,1] and its fuzzy subset is {VS, S, M, L, VL}, where VS, S, M, L, and VL denote very small, small, medium, large, and very large variable values, respectively.

In accordance with expert control experience and component characteristics, the fuzzy logic rules are designed as shown in Table 5. After the fuzzy calculation of battery and supercapacitor power, the HESS effective power value is found and transferred back to the upper-level controller input port until the optimal control sequence is obtained.

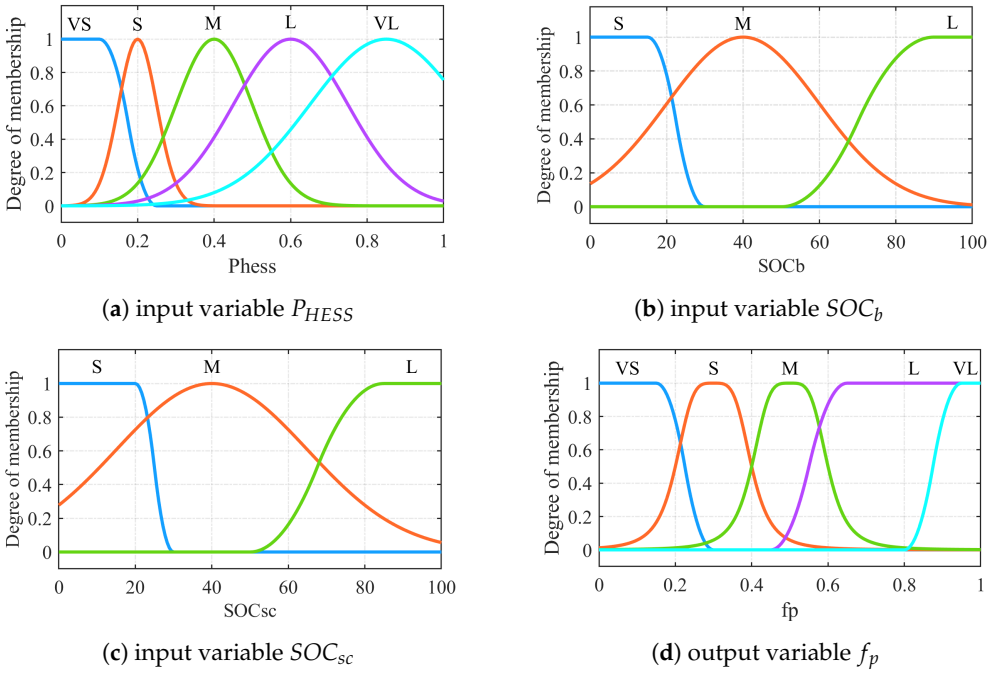

(**a**) input variable P_{HESS}

(**b**) input variable SOC_b

(**c**) input variable SOC_{sc}

(**d**) output variable f_p

Figure 10. Membership functions of input and output variables in FLC.

Table 5. Fuzzy logic control rules.

SOC_b	SOC_{sc}	P_{HESS}				
		VS	**S**	**M**	**L**	**VL**
SOC_b = S	S	VL	L	M	M	M
	M	VL	VL	L	L	M
	L	VL	VL	L	L	M
SOC_b = M	S	VL	VL	L	S	S
	M	VL	VL	VL	M	S
	L	VL	VL	L	M	S
SOC_b = L	S	VL	L	M	VS	VS
	M	VL	VL	L	M	S
	L	VL	VL	VL	L	M

5. Results and Discussion

5.1. Flight Mission Profile of HAGA

In order to better demonstrate the application potential of HAGA using a turbo-electric hybrid propulsion system, an air–ground amphibious mission profile is selected as the working condition. In the software simulation in Simcenter AMEsim, the simulation time is 3600 s with a set step size of 0.2 s. As shown in Figure 11, the flight mission profiles I and II include vertical take-off, cruise, vertical landing, and NEDC (New European Driving Cycle) phases. The NEDC consists of four urban cycles and one suburban cycle, the former at speeds up to 50 km/h and a maximum acceleration of 1.042 m/s^2, mainly consisting of idle, start, acceleration, and deceleration stop operations. The latter has a high speed of up to 120 km/h and a maximum acceleration of 0.833 m/s^2 [60].

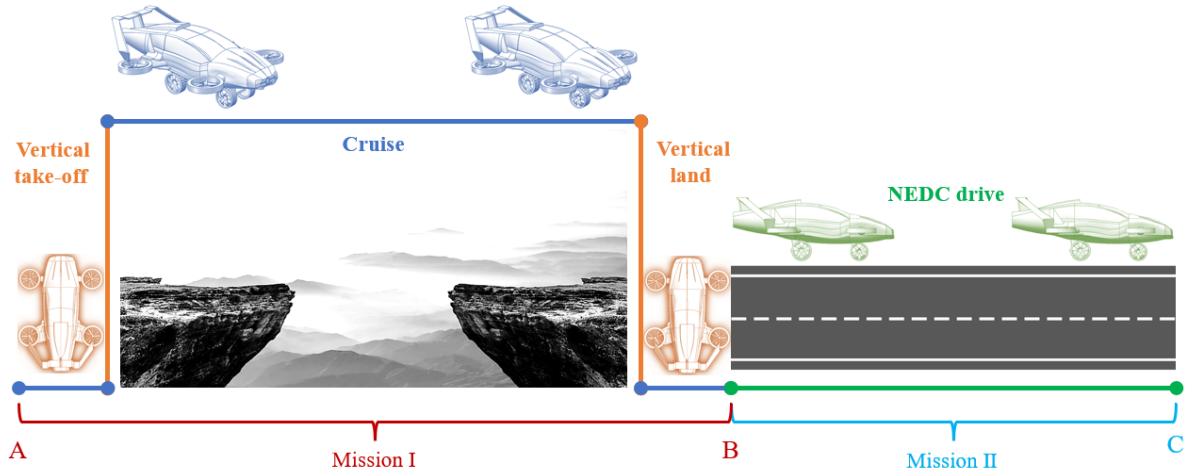

Figure 11. Flight mission profile for hybrid air–ground aircraft.

The corresponding speed and altitude curve can be seen in Figure 12a, where the vertical take-off phase has a Z-axis climb speed of 5 m/s, achieving a 900 m cruising flight altitude in 180 s, and the vertical landing speed of 3.8 m/s. The cruise flight speed is 60 m/s and the NEDC ground travel cycle simulates urban conditions with a maximum speed of 120 km/h. The ideal required power curve corresponding to the amphibious mission profile is obtained from the power analysis in the previous sector, where the required power for Mission I is large, but the change tendency is smooth, with the maximum required power during the vertical take-off phase at approximately 557 kW and the cruise power at approximately 258 kW. Additionally, the power for Mission II changes frequently, as shown in Figure 12b, with a maximum value of 187 kW at the highest drive speed.

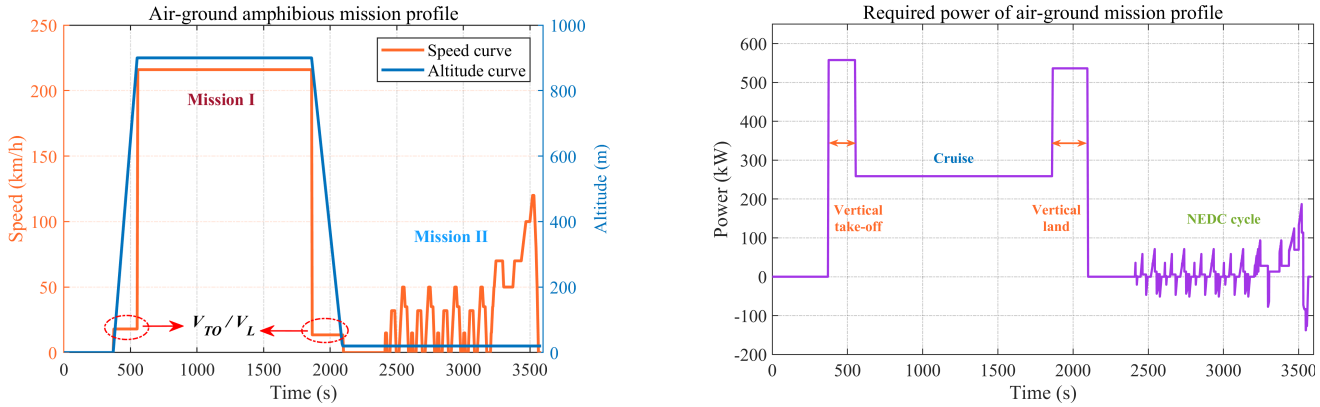

(**a**) speed and altitude curve (**b**) required power curve

Figure 12. Speed, altitude, and required power curve of HAGA in the air–ground amphibious mission.

5.2. Simulation Results and Analysis

According to the parameters of the HAGA's flight altitude, flight speed, and required power, a simulation platform for a turbine-electric hybrid propulsion system is established on the basis of Simceter AMEsim software. The feasibility of the application of the TEHPS and HESS on HAGA, the effectiveness of size optimization, and energy management strategy is explored at both general and partial indicators.

5.2.1. System-Level Analysis

The overall indicators cover parameters such as the output power of each subsystem, HESS energy and power ratio, total fuel consumption, and pollutant emissions. The required TEHPS power, TGS, and HESS provided are illustrated in Figure 13. During

phases such as vertical take-off and landing where the system required power is high, the TGS and HESS work together to supply power. At the start of the cruise phase, the SOC of the HESS is low and the turboshaft engine continues to maintain high power output until the SOC recovers in the high charge interval, after which only the engine provides demand power. In addition, the ground NEDC starts with less power, the turboshaft engine remains charged for the HESS, and when fully charged the engine adjusts its low power output to track the ground drive power requirement. Therefore, the HESS appropriately acts as a power buffer in the TEHPS, discharging at the VTOL phase to make up for the power lack and absorbing engine power to recharge itself during the first half cruise cycle and NEDC.

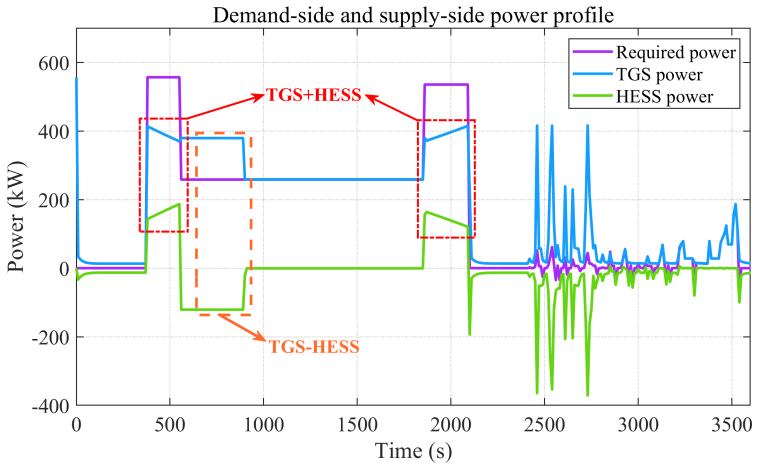

Figure 13. Demand-side and supply-side power profiles of the TEHPS.

The contribution of the hybrid energy storage system under the specific mission profile is measured in terms of the energy ratio and the power ratio, as shown in Figure 14. The former represents the ratio of HESS electrical energy to the total required energy, and the latter denotes the ratio of HESS output power to the required power for propulsion. It can be noted that the HESS can provide 10.85% of the overall energy, with a peak of 29% in terms of instantaneous energy ratio. The HESS output power ratio has a large value in the VTOL phase, with a maximum value of 33.56%, reflecting the importance of the HESS in the output energy and power of the TEHPS.

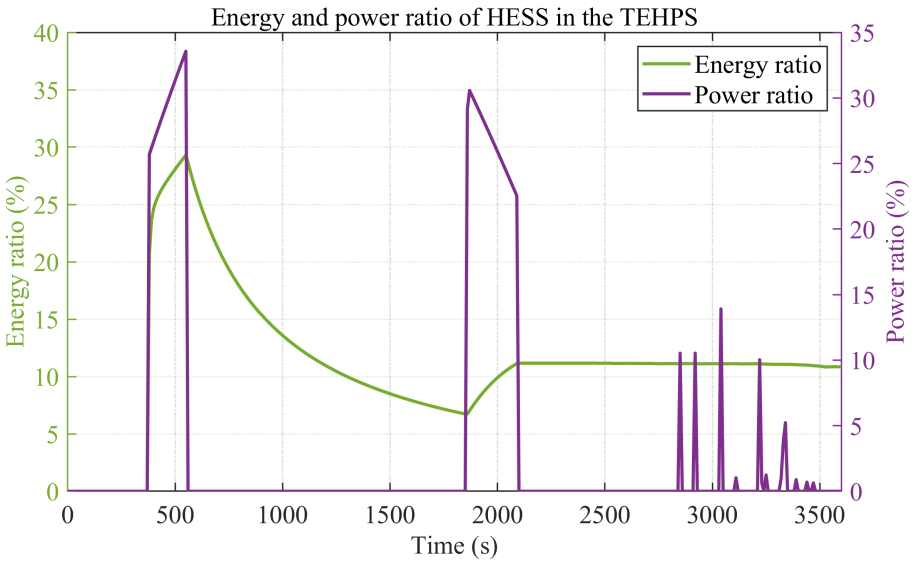

Figure 14. Energy and power ratios of HESS in the TEHPS under the air–ground amphibious mission.

The system-level evaluation metrics mainly reflect the overall fuel consumption and CO_2 emissions, and the fuel consumption curve of the hybrid and oil-powered AGA

under the air–ground amphibious mission profile are shown in Figure 15. The curves tend to increase linearly in segments, with a large slope and a significant increase in fuel consumption during the VTOL and cruise flight phases, and it increases slowly during the ground drive. Calculations show that the HAGA consumed 57.4 kg fuel under Mission I, with a total fuel consumption of 72.63 kg, however, the oil-powered AGA consumed 79.42 kg under Mission I, with a total fuel consumption of 92.88 kg.

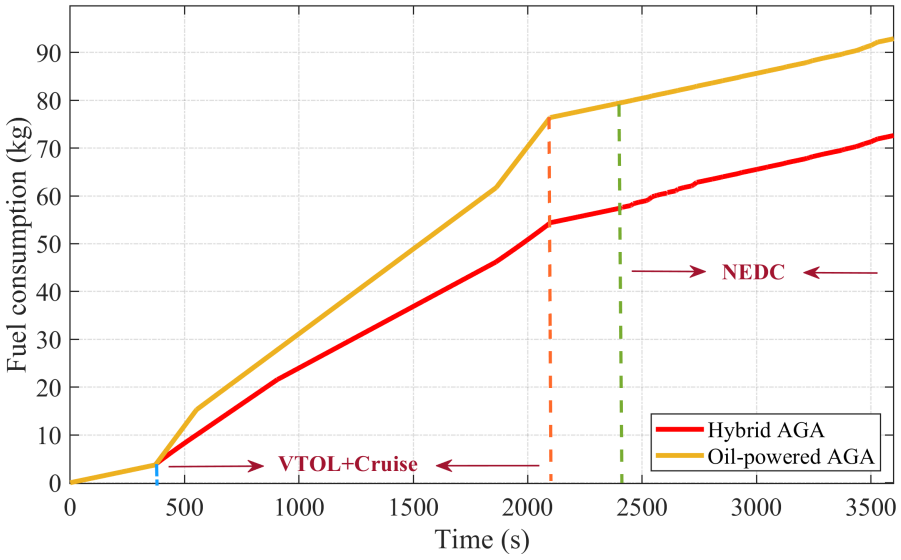

Figure 15. Fuel consumption comparison of the hybrid and oil-powered AGA under the air–ground amphibious mission.

To verify the potential of the hybrid combination form for air–ground aircraft applications, the total mass, fuel consumption, and pollutant emissions of a purely oil-powered aircraft are calculated for the identical mission and power level. The total weight of the oil-powered AGA can be estimated according to Equation (27), assuming the same structural mass factor and load mass. In contrast to the TEHPS, the oil-powered AGA powertrain involves a higher power turboshaft engine, multi-stage gearbox, and propulsion units, eliminating the generator, motors, hybrid energy storage system, and power electronics. Calculations show that the total mass of the oil-powered AGA powertrain is lighter at 1900 kg, a reduction of 10.53% compared to the TEHPS. Therefore, as shown in Table 6, a hybrid AGA can save 21.80% of fuel consumption and CO_2 emissions at a sacrifice of 10.53% of total weight compared to the oil-powered AGA, meeting the research objectives of energy saving and emission reduction.

Table 6. Total performance parameters of the TEHPS.

Type	Parameter	Value	Unit	Percent (%)
Oil-powered AGA	Fuel consumption	92.88	kg	-
	CO_2 emission	292.57	kg	-
	Total mass	1900	kg	-
Hybrid AGA	Fuel consumption	72.63	kg	−21.80%
	CO_2 emission	228.78	kg	−21.80%
	Total mass	2100	kg	+10.53%

5.2.2. Component-Level Analysis

For component-level metrics, the analysis concentrates on the operational status and performance advantages of the turboshaft engine and the hybrid energy storage system.

The turboshaft engine is the main power source of the TEHPS, incorporating several mechanical components and temperature control components. The power turbine is an essential mechanical component in the connection between the turboshaft engine and generator, so the dynamic characteristics of the turboshaft engine are characterized by analyzing its speed and torque curves. Setting the power turbine rotational speed at 20,600 rpm, the variation of its speed and torque for different output power of turboshaft engine is shown in Figure 16. The torque response follows the same trend as the power variation. Importantly, the power turbine operates at a constant speed during steady-state operation, and at a slight fluctuation rate during transient surges, which is beneficial for turbine life.

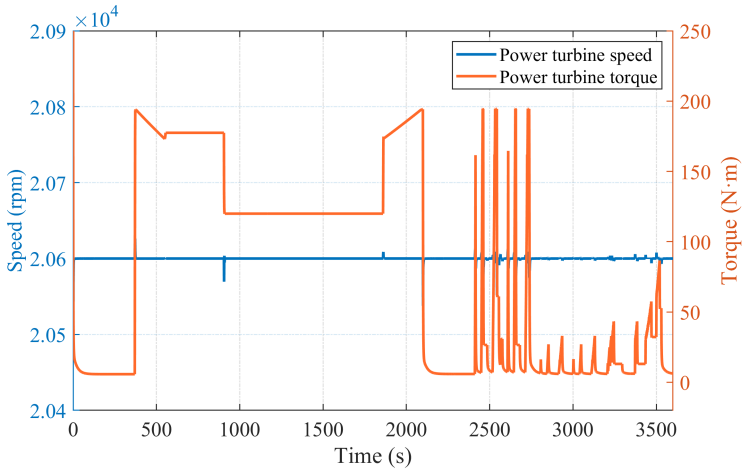

Figure 16. Speed and torque response curves of power turbine in the turboshaft engine.

The limits for the turbine entry temperature, exhaust gas temperature, and compressor discharge temperature are given in Section 2.1.1. As shown in Figure 17, the results demonstrate that the three profiles are consistent with the trend of the gas turbine power profile and stay within the maximum allowable range. Turbines, compressors, and combustion chamber temperatures below the preset values also indicate that the recuperated turboshaft engine can operate properly and respond quickly under the air–ground amphibious mission.

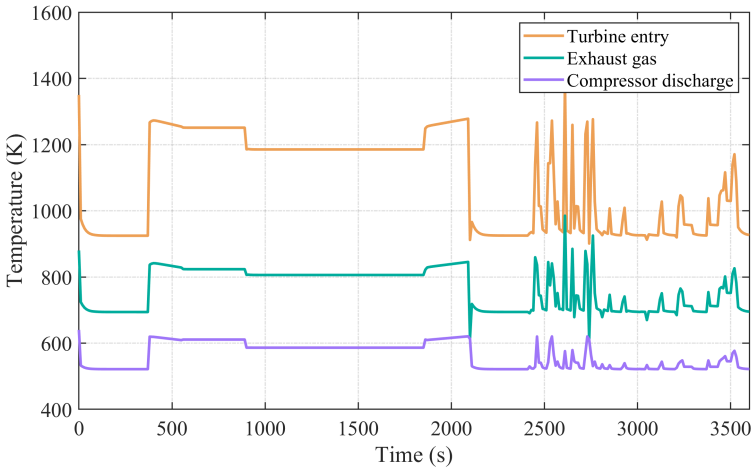

Figure 17. Temperature profile of turbine entry, exhaust gas, and compressor discharge in the turboshaft engine.

A comparison of the characteristics of single and hybrid energy storage in the TEHPS was conducted, involving the state of charge of each storage component and the trend of voltage and current profile. The SOC variation curve is shown in Figure 18, initial $SOC_{b/sc} = 80\%$, and the trend of the battery SOC_b variation in hybrid and single energy

storage systems is consistent, and both satisfy that the lower limit of SOC_b not less than 20%. The supercapacitor can respond instantaneously and quickly to the battery charge and discharge until the battery stabilizes input or output, which is evident during the VTOL and NEDC ground phases. In addition, due to the high power output of the turboshaft engine during the first half cycle of cruise and NEDC phases, the battery SOC_b is increased, and both the battery and supercapacitor charges reach reusable values at the end of the air–ground amphibious mission.

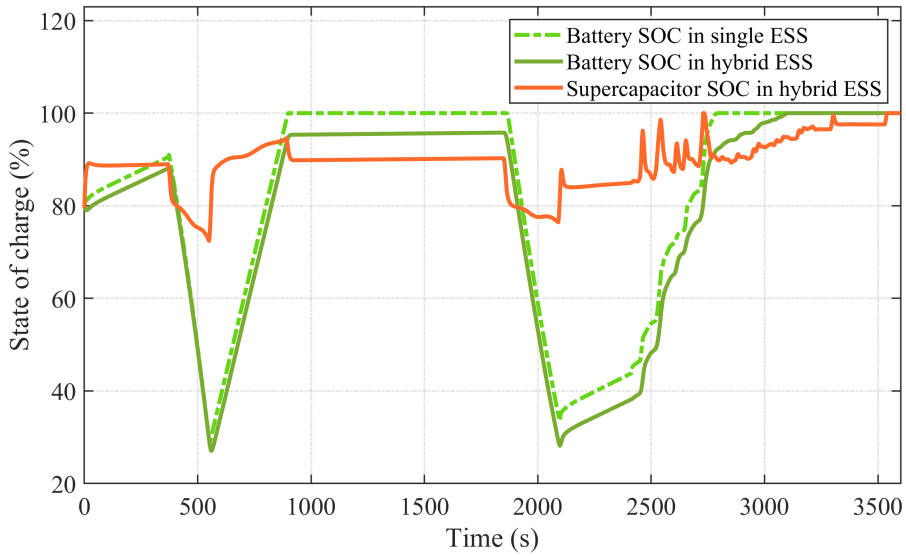

Figure 18. The SOC of energy storage devices in the single and hybrid ESS.

Specifically, the trend in voltage variation between the hybrid and single storage systems can be seen in Figure 19a, with a DC bus voltage of 800 V. The maximum fluctuation range of the DC bus voltage is 25% above and below the nominal value, so the data points are within the tolerance range. However, the number of battery transient charges and discharges is higher in the single ESS and the bus voltage oscillation is significant, which is detrimental to aircraft robustness. The current curve of the HESS can be observed in Figure 19b, and the supercapacitor pack can follow the trend of the required current when the current changes abruptly, providing a current with an amplitude of less than 100 A within 10 s. The battery pack has a response time of approximately 30 s, during which the load current is supplied together with the supercapacitor pack, which can reduce the impact of sudden high current on the battery and prolong its life cycle.

Moreover, due to the mass-sensitive nature of the aircraft, the comparison of the weight and volume characteristics in the single and hybrid energy storage systems is shown in Table 7. The results reveal that the combination form of battery and supercapacitor can reduce the total mass by 8.1% and the volume by 3.77% compared to a single battery pack, highlighting the energy and power density benefits of the HESS.

Table 7. Comparative analysis of energy storage system quality and volume.

Type	Storage	Weight	Volume	Total Weight	Percent	Total Volume	Percent
Single ESS	Battery	140 kg	69 L	140 kg	-	69 L	-
Hybrid ESS	Battery	87.5 kg	43.1 L	128.68 kg	−8.1%	66.4 L	−3.77%
	Supercapacitor	41.18 kg	23.3 L				

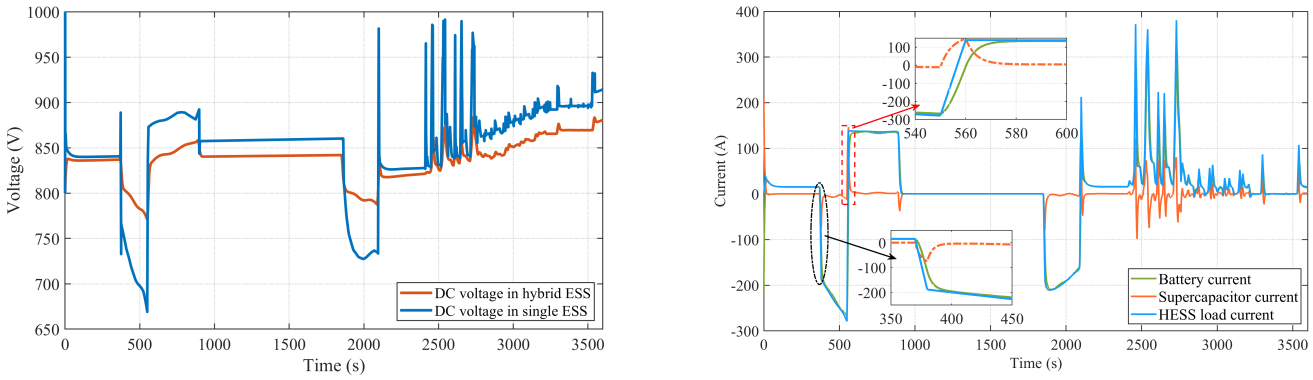

(**a**) voltage curve (**b**) current curve

Figure 19. Voltage and current curve of energy storage devices in the single and hybrid ESS.

6. Conclusions

Facing the electrification and energy-saving trends in the aviation industries, hybrid air–ground aircraft with air flight and ground driving capabilities is one of the promising solutions. This paper is dedicated to researching the architectural composition, sizing design, and energy management of an HAGA that can perform complex tasks such as VTOL and air–ground amphibious flight. The turbo-electric hybrid propulsion system has been determined based on a high-power turboshaft engine and a hybrid energy form of battery and supercapacitor, combined with the distributed electric drive-propulsion units. For the air–ground amphibious mission profile, power calculation, energy analysis, and weight estimation are carried out for the different flight phases. Owing to obtaining the optimum take-off weight and the best electric propulsion efficiency in the cruise phase, the design parameters including the number of battery and supercapacitor cells, the diameter and number of ducted fans, etc., are optimized iteratively based on a genetic algorithm. In addition, a top-down energy management framework has been developed to optimize fuel consumption and pollutant emissions, applying the ECMS and FLC methods to system-level and component-level energy management, respectively. Simulation results show that the TEHPS applying the above size design and energy management strategies can achieve a 21.80% reduction in fuel consumption and CO_2 emissions at the expense of a 10.53% increase in the whole aircraft mass, compared to the oil-only powertrain system. Moreover, the critical temperature parameters TET, EGT, and CDT of the turboshaft engine are in line with the trend of the power curve and within the threshold range. The hybrid energy storage system can account for up to 29% and 33.56% of the energy and power ratio in the TEHPS, and it is feasible to reduce the mass by 8.1% and the volume by 3.77% compared to the single ESS while reducing voltage fluctuation and maintaining stability. The proposed system configuration, sizing methodology, and energy management control strategies can provide the theoretical basis for the wider application of HAGA in the future. A comparative analysis of existing sizing optimization methods and energy management strategies for multiple profiles will be presented later to determine the best option for HAGA.

Author Contributions: Conceptualization and methodology, M.B. and W.Y.; software, M.B.; validation, J.L.; formal analysis, M.B.; investigation, M.K. (Marek Kosuda); resources, W.Y. and J.L.; data curation, M.B.; writing—original draft preparation, M.B.; writing—review and editing, M.B. and L.F.; visualization, M.K. (Miroslav Kelemen); supervision, W.Y. and M.K. (Miroslav Kelemen). All authors have read and agreed to the published version of the manuscript.

Funding: This research received no external funding.

Institutional Review Board Statement: Not applicable.

Informed Consent Statement: Not applicable.

Data Availability Statement: Not applicable.

Conflicts of Interest: The authors declare no conflict of interest.

Abbreviations

The following abbreviations are used in this manuscript:

HAGA	Hybrid Air–Ground Aircraft
TEHPS	Turbo-Electric Hybrid Propulsion System
TGS	Turbine Generation System
HESS	Hybrid Energy Storage System
ADEPS	Air-Distributed Electric Propulsion System
GDEDS	Ground-Distributed Electric Drive System
VTOL	Vertical Take-Off and Landing
NEDC	New European Driving Cycle
GA	Genetic Algorithm
EMS	Energy Management Strategy
ECMS	Equivalent Consumption Minimum Strategy
SOC	State Of Charge
TET	Turbine Entry Temperature
EGT	Exhaust Gas Temperature
CDT	Compressor Discharge Temperature

References

1. Bruner, S.; Baber, S.; Harris, C.; Caldwell, N.; Keding, P.; Rahrig, K.; Pho, L.; Wlezian, R. *NASA N+3 Subsonic Fixed Wing Silent Efficient Low-Emissions Commercial Transport (SELECT) Vehicle Study*; NASA: Washington, DC, USA, 2010.
2. Krein, A.; Williams, G. Flightpath 2050: Europe's vision for aeronautics. In *Innovation for Sustainable Aviation in a Global Environment, Proceedings of the Sixth European Aeronautics Days, Madrid, Spain, 30 March–1 April 2012*; IOS Press: Amsterdam, The Netherlands, 2012.
3. Wang, Y.; Guo, C.H.; Chen, X.J.; Jia, L.Q.; Guo, X.N.; Chen, R.S.; Zhang, M.S.; Chen, Z.Y.; Wang, H.D. Carbon peak and carbon neutrality in China: Goals, implementation path and prospects. *China Geol.* **2021**, *4*, 720–746. [CrossRef]
4. Rajashekara, K.; Wang, Q.; Matsuse, K. Flying cars: Challenges and propulsion strategies. *IEEE Electrif. Mag.* **2016**, *4*, 46–57. [CrossRef]
5. Ahmed, S.S.; Hulme, K.F.; Fountas, G.; Eker, U.; Benedyk, I.V.; Still, S.E.; Anastasopoulos, P.C. The flying car—Challenges and strategies toward future adoption. *Front. Built Environ.* **2020**, *6*, 106. [CrossRef]
6. Postorino, M.N.; Sarné, G.M.L. Reinventing mobility paradigms: Flying car scenarios and challenges for urban mobility. *Sustainability* **2020**, *12*, 3581. [CrossRef]
7. Pan, G.; Alouini, M.S. Flying car transportation system: Advances, techniques, and challenges. *IEEE Access* **2021**, *9*, 24586–24603. [CrossRef]
8. Vahana: Our Single-Seat eVTOL Demonstrator. Available online: https://www.airbus.com/en/urbanairmobility/cityairbus-nextgen/vahana (accessed on 19 October 2022).
9. CityAirbus NextGen. Available online: https://www.airbus.com/en/innovation/zero-emission/urban-air-mobility/cityairbus-nextgen (accessed on 19 October 2022).
10. Electric Aerial Ridesharing. Available online: https://www.jobyaviation.com/ (accessed on 19 October 2022).
11. Terrafugia Inc. Launches New Brand and Commercial UAV. Available online: https://terrafugia.com/all/terrafugia-inc-launches-new-brand-and-commercial-uav/ (accessed on 19 October 2022).
12. Bell Reveals a Surprisingly Down-to-Earth Air Taxi. Available online: https://www.wired.com/story/bell-nexus-air-taxi-flying-car/ (accessed on 19 October 2022).
13. WD-1. Available online: https://detroitflyingcars.com/specifications/ (accessed on 19 October 2022).
14. Friedrich, C.; Robertson, P. Hybrid-electric propulsion systems for aircraft. In Proceedings of the 11th International Energy Conversion Engineering Conference, San Jose, CA, USA, 14–17 July 2013; p. 3806.
15. Ye, X.I.; Savvarisal, A.; Tsourdos, A.; Zhang, D.; Jason, G.U. Review of hybrid electric powered aircraft, its conceptual design and energy management methodologies. *Chin. J. Aeronaut.* **2021**, *34*, 432–450.
16. Bravo, G.M.; Praliyev, N.; Veress, Á. Performance analysis of hybrid electric and distributed propulsion system applied on a light aircraft. *Energy* **2021**, *214*, 118823. [CrossRef]
17. Snyder, C.A.; Tong, M.T. Modeling turboshaft engines for the revolutionary vertical lift technology project. In Proceedings of the Annual Forum and Technology Display: The Future of Vertical Flight (GRC-E-DAA-TN66991), Philadelphia, PA, USA, 13–16 May 2019.

18. Petrochenkov, A.B.; Romodin, A.V.; Leizgold, D.Y.; Semenov, A.S. Modeling power-supply systems with gas-turbine units as energy sources. *Russ. Electr. Eng.* **2020**, *91*, 673–680. [CrossRef]
19. Donateo, T.; Cucciniello, L.; Strafella, L.; Ficarella, A. Control oriented modelling of a turboshaft engine for hybrid electric urban air-mobility. In Proceedings of the E3S Web of Conferences, Rome, Italy, 15–16 September 2020; EDP Sciences: Les Ulis, France, 2020; Volume 197, p. 05003.
20. Alrashed, M.; Nikolaidis, T.; Pilidis, P.; Jafari, S. Utilisation of turboelectric distribution propulsion in commercial aviation: A review on NASA's TeDP concept. *Chin. J. Aeronaut.* **2021**, *34*, 48–65. [CrossRef]
21. Campagna, N.; Castiglia, V.; Damiano, A.; Di Noia, L.P.; Miceli, R.; Di Tommaso, A.O.. A Hybrid Energy Storage Sizing for a Vertical Take-off and Landing Electric Aircraft. In Proceedings of the IECON 2021–47th Annual Conference of the IEEE Industrial Electronics Society, Toronto, ON, Canada, 13–16 October 2021; pp. 1–6.
22. Cheng, L.; Zhang, F.; Liu, S.; Zhang, Z. Configuration method of hybrid energy storage system for high power density in More Electric Aircraft. *J. Power Sources* **2020**, *445*, 227322. [CrossRef]
23. Li, J.; Zou, W.; Yang, Q.; Yi, F.; Bai, Y.; Wei, Z.; He, H. Size optimization and power allocation of a hybrid energy storage system for frequency service. *Int. J. Electr. Power Energy Syst.* **2022**, *141*, 108165. [CrossRef]
24. Li, J.; Sun, T.; Huang, X.; Ma, L.; Lin, Q.; Chen, J.; Leung, V.C. A memetic path planning algorithm for unmanned air/ground vehicle cooperative detection systems. *IEEE Trans. Autom. Sci. Eng.* **2021**, *19*, 2724–2737. [CrossRef]
25. Zhao, J.; Yang, C.; Wang, W.; Xu, B.; Li, Y.; Yang, L.; Zhu, H.; Xiang, C. A game-learning-based smooth path planning strategy for intelligent air-ground vehicle considering mode switching. *IEEE Trans. Transp. Electrif.* **2022**. [CrossRef]
26. Dai, H.; Bian, H.; Li, C.; Wang, B. UAV-aided wireless communication design with energy constraint in space-air-ground integrated green IoT networks. *IEEE Access* **2020**, *8*, 86251–86261. [CrossRef]
27. Liu, X.; Wu, Y.; Duan, J. Optimal sizing of a series hybrid electric vehicle using a hybrid genetic algorithm. In Proceedings of the 2007 IEEE International Conference on Automation and Logistics, Jinan, China, 18–21 August 2007; pp. 1125–1129.
28. Xie, Y.; Savvaris, A.; Tsourdos, A. Sizing of hybrid electric propulsion system for retrofitting a mid-scale aircraft using non-dominated sorting genetic algorithm. *Aerosp. Sci. Technol.* **2018**, *82*, 323–333. [CrossRef]
29. Economou, J.T.; Tsourdos, A.; Wang, S. Design of a distributed hybrid electric propulsion system for a light aircraft based on genetic algorithm. In Proceedings of the AIAA Propulsion and Energy 2019 Forum, Indianapolis, IN, USA, 19–22 August 2019; p. 4305.
30. De Vries, R.; Brown, M.; Vos, R. Preliminary sizing method for hybrid-electric distributed-propulsion aircraft. *J. Aircr.* **2019**, *56*, 2172–2188. [CrossRef]
31. Finger, D.F.; Bil, C.; Braun, C. Initial sizing methodology for hybrid-electric general aviation aircraft. *J. Aircr.* **2020**, *57*, 245–255. [CrossRef]
32. Finger, D.F.; Götten, F.; Braun, C.; Bil, C. Mass, primary energy, and cost: The impact of optimization objectives on the initial sizing of hybrid-electric general aviation aircraft. *CEAS Aeronaut. J.* **2020**, *11*, 713–730. [CrossRef]
33. Chakraborty, I.; Miller, N.S.; Mishra, A.A. Sizing and Analysis of a Tilt-Wing Aircraft with All-Electric and Hybrid-Electric Propulsion Systems. In Proceedings of the AIAA SCITECH 2022 Forum, San Diego, CA, USA, 3–7 January 2022; p. 1515.
34. Chakraborty, I.; Mishra, A.A.; Miller, N.S.; Dommelen, D.V.; Anemaat, W.A. Design and Sizing of a Dual-Purpose Hybrid-Electric Ducted Fan Lift-Plus-Cruise Aircraft. In Proceedings of the AIAA SCITECH 2022 Forum, San Diego, CA, USA, 3–7 January 2022; p. 1516.
35. Lee, D.; Lim, D.; Yee, K. Generic Design Methodology for Vertical Takeoff and Landing Aircraft with Hybrid-Electric Propulsion. *J. Aircraft* **2022**, *59*, 278–292. [CrossRef]
36. Wang, W.; Chen, Y.; Yang, C.; Li, Y.; Xu, B.; Huang, K.; Xiang, C. An efficient optimal sizing strategy for a hybrid electric air-ground vehicle using adaptive spiral optimization algorithm. *J. Power Sources* **2022**, *517*, 230704. [CrossRef]
37. Wang, W.; Chen, Y.; Yang, C.; Li, Y.; Xu, B.; Xiang, C. An enhanced hypotrochoid spiral optimization algorithm based intertwined optimal sizing and control strategy of a hybrid electric air-ground vehicle. *Energy* **2022**, *2022*, 124749. [CrossRef]
38. Ma, R.; Yuan, M.; Zhou, Y.; Zhang, Y.; Yang, F. Energy Management Strategy of Distributed Electric Propulsion Aircraft Hybrid Power System based on State Machine. In Proceedings of the IECON 2021–47th Annual Conference of the IEEE Industrial Electronics Society, Toronto, ON, Canada, 13–16 October 2021; pp. 1–6.
39. Han, K.; Qian, H.; Zhang, Q.; Liu, L.; Hu, X. Optimization of energy management system for fuel-cell/battery hybrid power in unmanned aerial vehicle. In Proceedings of the 2019 22nd International Conference on Electrical Machines and Systems (ICEMS), Harbin, China, 11–14 August 2019; pp. 1–6.
40. Zhang, X.; Liu, L.; Dai, Y.; Lu, T. Experimental investigation on the online fuzzy energy management of hybrid fuel cell/battery power system for UAVs. *Int. J. Hydrogen Energy* **2018**, *43*, 10094–10103. [CrossRef]
41. Donateo, T.; Terragno, A.; Ficarella, A. An optimized fuzzy logic for the energy management of a hybrid electric air-taxi. *E3S Web Conf.* **2021**, *312*, 07004.
42. Donateo, T.; De Pascalis, C.L.; Strafella, L.; Ficarella, A. Off-line and on-line optimization of the energy management strategy in a Hybrid Electric Helicopter for urban air-mobility. *Aerosp. Sci. Technol.* **2021**, *113*, 106677. [CrossRef]
43. Donateo, T.; de Pascalis, C.L.; Strafella, L.; Ficarella, A. Optimal Energy Management of a Hybrid Electric Helicopter for Urban Air-Mobility. In Proceedings of the IOP Conference Series: Materials Science and Engineering, Sanya, China, 12–14 November 2021; IOP Publishing: Bristol, UK, 2021; Volume 1024, p. 012074.

44. Misley, A.; D'Arpino, M.; Ramesh, P.; Canova, M. A real-time energy management strategy for hybrid electric aircraft propulsion systems. In Proceedings of the 2021 AIAA/IEEE Electric Aircraft Technologies Symposium (EATS), San Diego, CA, USA, 12–16 June 2021; pp. 1–11.
45. Doff-Sotta, M.; Cannon, M.; Bacic, M. Predictive energy management for hybrid electric aircraft propulsion systems. *IEEE Trans. Control Syst. Technol.* **2022**. [CrossRef]
46. Xie, Y.; He, S.; Savvaris, A.; Tsourdos, A.; Zhang, D.; Xie, A.. Convexification in energy optimization of a hybrid electric propulsion system for aerial vehicles. *Aerosp. Sci. Technol.* **2022**, *123*, 107509. [CrossRef]
47. Wei, Z.; Ma, Y.; Xiang, C.; Liu, D. Power Prediction-Based Model Predictive Control for Energy Management in Land and Air Vehicle with Turboshaft Engine. *Complexity* **2021**, *2021*, 2953241. [CrossRef]
48. Zhu, J.; Chen, L.; Wang, X.; Yu, L. Bi-level optimal sizing and energy management of hybrid electric propulsion systems. *Appl. Energy* **2020**, *260*, 114134. [CrossRef]
49. Xie, Y.; Savvaris, A.; Tsourdos, A. Fuzzy logic based equivalent consumption optimization of a hybrid electric propulsion system for unmanned aerial vehicles. *Aerosp. Sci. Technol.* **2019**, *85*, 13–23. [CrossRef]
50. Bai, M.; Yang, W.; Song, D.; Kosuda, M.; Kelemen, M. Equivalent Consumption Minimization Strategy based on fuzzy logic control for the energy management of hybrid Unmanned Aerial Vehicle. In Proceedings of the International Conference on Applied Energy 2021, Virtual, 29 November–5 December 2021.
51. Roumeliotis, I.; Nikolaidis, T.; Pachidis, V.; Broca, O.; Unlu, D. Dynamic simulation of a rotorcraft hybrid engine in Simcenter Amesim. In Proceedings of the European Rotorcraft Forum, Delft, The Netherlands, 18–21 September 2018.
52. Ballin, M.G. *A High Fidelity Real-Time Simulation of a Small Turboshaft Engine*; NASA: Washington, DC, USA, 1988.
53. Khaligh, A.; Li, Z. Battery, ultracapacitor, fuel cell, and hybrid energy storage systems for electric, hybrid electric, fuel cell, and plug-in hybrid electric vehicles: State of the art. *IEEE Trans. Veh. Technol.* **2010**, *59*, 2806–2814. [CrossRef]
54. Schiffer, J.; Linzen, D.; Sauer, D.U. Heat generation in double layer capacitors. *J. Power Sources* **2006**, *160*, 765–772. [CrossRef]
55. Dekterev, A.A.; Dekterev, A.A.; Dekterev, D.A.; Goryunov, Y.N. Investigation of the effects of end faces design on parameters of cycloidal rotor. In *Journal of Physics: Conference Series*; IOP Publishing: Bristol, UK, 2018; Volume 1105, p. 012029.
56. Mahmuddin, F. Rotor blade performance analysis with blade element momentum theory. *Energy Procedia* **2017**, *105*, 1123–1129. [CrossRef]
57. Tyan, M.; Van Nguyen, N.; Kim, S.; Lee, J.W. Comprehensive preliminary sizing/resizing method for a fixed wing–VTOL electric UAV. *Aerosp. Sci. Technol.* **2017**, *71*, 30–41. [CrossRef]
58. Zong, J.; Zhu, B.; Hou, Z.; Yang, X.; Zhai, J. Evaluation and comparison of hybrid wing VTOL UAV with four different electric propulsion systems. *Aerospace* **2021**, *8*, 256. [CrossRef]
59. Onori, S.; Serrao, L.; Rizzoni, G. *Hybrid Electric Vehicles: Energy Management Strategies*; Springer: Berlin, Germany, 2015.
60. Armas, O.; García-Contreras, R.; Ramos, Á. Impact of alternative fuels on performance and pollutant emissions of a light duty engine tested under the new European driving cycle. *Appl. Energy* **2013**, *107*, 183–190. [CrossRef]